



Comprehensive evaluation of iAMAS (v1.0) in simulating Antarctic meteorological fields with observations and reanalysis

Qike Yang¹, Chun Zhao^{1,2,3,*}, Jiawang Feng¹, Gudongze Li¹, Jun Gu¹, Zihan Xia¹, Mingyue Xu¹, and Zining Yang¹

¹Deep Space Exploration Laboratory / School of Earth and Space Sciences / CMA-USTC Laboratory of Fengyun Remote Sensing / State Key Laboratory of Fire Science / Institute of Advanced Interdisciplinary Research on High-Performance Computing Systems and Software, University of Science and Technology of China, Hefei 230026, China

²Laoshan Laboratory, Qingdao, China

³CAS Center for Excellence in Comparative Planetology, University of Science and Technology of China, Hefei, China

Correspondence: Chun Zhao (chunzhao@ustc.edu.cn)

Abstract. Regular latitude-longitude grids in global simulations encounter polar singularities in the Arctic and Antarctic regions. In contrast, unstructured meshes have the potential to overcome this issue; however, so far, the performance of unstructured meshes in polar areas is barely investigated. This study examined the efficacy of unstructured meshes over Antarctica using the integrated Atmospheric Model Across Scales (iAMAS, v1.0) with multi-source observations. Four mesh configurations of the iAMAS model were assessed, varying in resolutions (120 km, 60 km, 16 km, and 4 km) over the Antarctic region. The study evaluates the iAMAS simulation performance for both surface layer and upper meteorological fields (temperature, pressure, specific humidity, and wind speed), by comparing simulations against the fifth-generation ECMWF reanalysis (ERA5) data and measurements from automatic weather stations and radiosondes. The results indicate that the iAMAS model does not exhibit the polar singularity issue observed in ERA5, where the ERA5 with regular latitude-longitude grids significantly underestimates wind speeds at the polar grid center (i.e., the South Pole at 90°S). In the relatively flat region of East Antarctica, all four iAMAS experiments at various resolutions demonstrate comparable and even superior performance in simulating temperature and wind speed when compared to ERA5. In regions with complex terrain, such as near the Transantarctic Mountains, the iAMAS model (particularly at coarse grid resolutions like 120 km) exhibits a cold bias and stronger wind speeds, consistent with biases identified in other Antarctic simulations using regional models with latitude-longitude grids. Notably, mesh refinement at 4 km in complex terrains significantly enhance iAMAS's accuracy in simulating the meteorological fields for both the surface layer and upper atmosphere, suggesting that a grid resolution of 4 km (or even higher) is optimal in such regions. Conversely, in flatter areas, like the high East Antarctic plateau, increases in grid resolution yield minimal improvements in simulation accuracy, and a 60-km grid resolution appears sufficient.

1 Introduction

The Antarctic continent is the highest, driest, and coldest region on Earth, providing a unique environment for testing atmospheric models under extreme conditions. Furthermore, this distinctive environment facilitates a range of sophisticated sci-



tific experiments, including ice-core records of climate properties (Petit et al., 1999), assessments of Antarctic contributions to future sea-level rise (Golledge et al., 2015), investigations into the role of ice sheets in the global carbon cycle (Wadham et al., 2019), and studies on Antarctic ozone holes (Kessenich et al., 2023). Additionally, increases in surface temperature are expected to be amplified in polar regions (Clem et al., 2020; Douville, 2023), and the effects of Antarctic amplification have garnered significant attention (Wang et al., 2021; Gao et al., 2019). Consequently, Antarctic simulations are crucial, as they provide the necessary meteorological fields for analyzing the above Antarctic implications and offer critical weather predictions for scheduling relevant scientific field campaigns.

In Antarctica, the regular latitude-longitude (or rectangular/square) grid used in atmospheric models suffers from the issue of polar singularities, where lines of longitude converge at the poles within a global grid framework (Collins et al., 2013). Then the regular latitude-longitude grid is the most commonly used configuration in regional atmospheric models (e.g., the Weather Research and Forecasting (WRF) Model; Skamarock et al., 2008). As for global model, the application of unstructured meshes (e.g., Voronoi meshes; Skamarock et al., 2012) was proposed as a method to avoid polar singularities.

However, studies on the performance of unstructured meshes for simulating high latitudes (or polar regions) are limited, as the meteorological fields (temperature, pressure, humidity, and wind) simulated by global models using unstructured meshes have primarily been evaluated at mid-latitudes (Ha et al., 2018; Hsu et al., 2020; Imberger et al., 2021; Lui et al., 2020; Núñez Ocasio and Rios-Berrios, 2023; Pilon et al., 2016; Schwartz, 2019; Zhao et al., 2019; Xu et al., 2021, 2024). Therefore, this study investigates the performance of unstructured meshes over polar regions, specifically Antarctica, using a global atmospheric model known as the integrated Atmospheric Model Across Scales (iAMAS, v1.0).

The iAMAS (Gu et al., 2022) is a non-hydrostatic atmospheric model developed using the new Sunway heterogeneous-architecture High-Performance Computing (HPC) system. It is based on the dynamic core of Model for Prediction Across Scales for Atmosphere (MPAS-Atmosphere; Skamarock et al., 2012), which employs Spherical Centroidal Voronoi Tessellations (SCVT) and C-grid discretization (Ringler et al., 2010; Skamarock et al., 2012; Thuburn et al., 2009). SCVTs facilitate the discretization of a sphere into a highly uniform mesh (Ringler et al., 2008, 2011), thereby avoiding the polar singularity issues associated with regular latitude-longitude grids. Furthermore, the variable-resolution meshes of iAMAS enable high-resolution regional refinement without the necessity for grid nesting.

This study evaluates the simulation capabilities of iAMAS in Antarctica and analyzes its shortcomings and relevant potential reasons. This is crucial for understanding the simulation characteristics of unstructured meshes in polar regions. This study aims to provide a foundational analysis of model performance to guide future improvements to iAMAS in polar regions and to inspire the application of other unstructured mesh atmospheric models in this areas.

This study evaluates the simulation skill of iAMAS for Antarctic meteorological fields, including temperature, pressure, humidity, and wind. Four global mesh configurations with varying resolutions (120 km, 60 km, 16 km, and 4 km) over the Antarctic region are employed to investigate the effects of regional refinement on model performance. The iAMAS simulations were initialized using a global atmospheric reanalysis produced by the European Centre for Medium-range Weather Forecasts (ECMWF), specifically the fifth-generation ECMWF reanalysis data (ERA5; Hersbach et al., 2020).



This study compares iAMAS simulations with Antarctic measurements. Surface measurements are obtained from Automatic Weather Stations (AWS), while upper-air measurements are collected from radiosondes. ERA5 data are also utilized for comparison, which helps assess whether the simulation bias is influenced by the initial conditions (i.e., ERA5) or by iAMAS itself. Additionally, the statistical results from ERA5, evaluated against observed data, can serve as an evaluation reference for the performance of iAMAS. Sect. 2 describes the model and experiment design, the observations and reanalysis data sets. In Sect. 3, the iAMAS model performance in simulating meteorological fields in Antarctica and the potential reasons for model biases are investigated. The conclusions and discussions are provided in Sect. 4.

2 Methodology

2.1 Model and experiments

2.1.1 iAMAS

The numerical experiments in this study are conducted using the iAMAS model, which is a atmospheric model with unstructured meshes with the capability of regional refinement. Its non-hydrostatic dynamical core is based on MPAS-Atmosphere, and discretizes the computational domain horizontally on a C-grid staggered SCVT mesh (Skamarock et al., 2012). The SCVT generation algorithms can produce global quasi-uniform resolution meshes and variable-resolution meshes through a density function (Ju et al., 2011). The atmospheric solver in iAMAS employs fully compressible non-hydrostatic equations. To solve these equations of motion, a terrain-following coordinate system with smoothed surfaces (Klemp, 2011) and a split-explicit third-order Runge-Kutta time integration scheme were utilized (Dudhia et al., 2007; Wicker and Skamarock, 2002).

The iAMAS model, developed by our research group (e.g., Gu et al., 2022; Hao et al., 2023; Feng et al., 2023), incorporates several coding optimizations, including multi-dimensional parallelism, aggressive and fine-grained optimization, manual vectorization, and parallelized I/O fragmentation up on the many-core heterogeneous-architecture of the China Sunway HPC platform. iAMAS is a coupled meteorology and chemistry model that can simulate online emission, advection, diffusion, vertical turbulent mixing, dry deposition, gravitational settling, wet scavenging processes, optical averaging, species-related transport, aerosol-radiation and aerosol-cloud interactions (Feng et al., 2023). The physical parameterizations (e.g., radiative, microphysics, land surface, and boundary layer) are implemented into the model and coupled with dynamical core (Gu et al., 2022) up on the structure of the Sunway HPC as well. The physical schemes employed in this study will be introduced later (Sect. 2.1.2). As a result of these significant efforts, the iAMAS model is already being applied scientific researches in atmospheric modeling (Gu et al., 2024), and indicating that regional refinement covering the area of interest can improve the simulation capability. Based on the China Sunway HPC platform, global simulations with uniform resolution were carried out using iAMAS (Zhang et al., 2023), and found the largest differences between the 3-km and 60-km resolution iAMAS simulations regarding atmospheric temperatures and winds occur in the Antarctic region. This significant variation in the performance of iAMAS with different resolutions in Antarctica also serves as a key motivation for iAMAS simulations in this region.



Antarctica has the cleanest air on Earth, as there are fewer people using industrial chemicals and burning fossil fuels. Therefore, this study employs the iAMAS model without activating the chemistry suite and primarily evaluates routine meteorological fields (temperature, pressure, humidity, and wind) over Antarctica. However, some aerosols (e.g., black carbon; Kannemadugu et al., 2023) have shown an increasing trend in Antarctica in recent years, suggesting that future simulations for Antarctic aerosols may be warranted with this model.

2.1.2 Numerical experiments

Four sets of experiments were conducted with different mesh structures: two quasi-uniform resolution meshes and two variable-resolution meshes. The quasi-uniform meshes have grid spacings of approximately 120 km (U120km) and 60 km (U60km). The first variable-resolution mesh features a circular high-resolution region with a grid spacing of 16 km (V16km), centered over the South Pole (90°S, -°E), where the 16-km mesh region (from 90°S to 60°S) encompasses the entire Antarctic continent. The second variable-resolution mesh also features a circular refined region but with a 4-km resolution (V4km), centered at 80°S, 160°E. This 4-km resolution refinement has a diameter of 2500 km and nearly covers the entire Transantarctic Mountains with complex terrain. The variable-resolution meshes (V16km and V4km) include transition zones between fine and coarse resolutions, with both V16km and V4km having a resolution of approximately 60 km outside their transition regions. These four meshes are illustrated in Fig. 1 and are used to assess the impact of model grid resolution on Antarctic simulations. Detailed information on the four meshes utilized in the experiments is summarized in Table 1. The time step should be smaller for finer grid spacing, as indicated by the Courant-Friedrichs-Lewy rule. The time steps for U120km, U60km, V16km, and V4km are set at 600 s, 300 s, 80 s, and 20 s, respectively.

Table 1. Characteristics of four meshes in the experiments.

Mesh	Resolution of refinement	Center of refinement	Diameter of refinement	numbers of mesh cells
U120km	-	-	-	~0.04 million
U60km	-	-	-	~0.16 million
V16km	16 km	90°S, -°E	~6700 km	~0.31 million
V4km	4 km	80°S, 160°E	~2500 km	~0.79 million

The iAMAS model is configured with 55 vertical layers and a model top at 30 km. The initial conditions for iAMAS were derived from ERA5 reanalysis data. The first 24 hours are considered the initial spin-up period; only simulations from 24 to 120 hours are combined to create a continuous time series for monthly analyses. The four iAMAS experiments (U120km, U60km, V16km, and V4km) were conducted over four months (January, April, July, and October) in 2015, representing the four seasons. In Antarctica, the seasons do not exhibit the distinct characteristics found in the mid-latitudes. In this study, January and October, which fall within the Antarctic polar day, are regarded as warm months, while April and July, occurring during the polar night, are considered cold months. The main physical schemes employed in this study are detailed in Table 2, which presents the common configurations for the four iAMAS experiments configured with different grid resolutions.

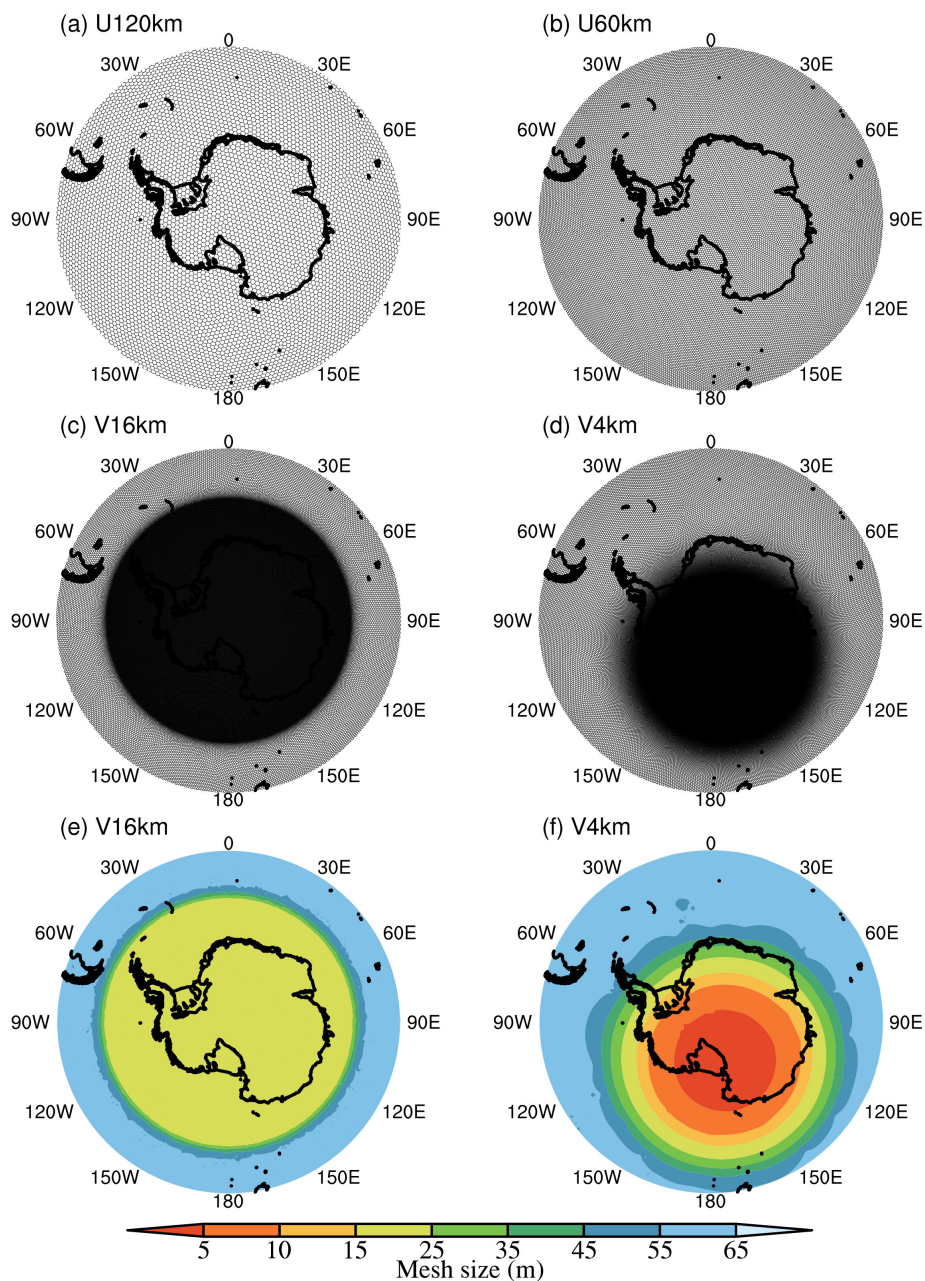


Figure 1. (a) Global quasi-uniform resolution mesh with a grid spacing of 120 km (U120km). (b) Global quasi-uniform resolution mesh with a grid spacing of 60 km (U60km). (c) Global variable-resolution mesh with a grid spacing ranging from 16 km to 60 km (V16km), featuring a refined region over the entire Antarctic continent. (d) Global variable-resolution mesh with a grid spacing ranging from 4 km to 60 km (V4km), featuring a refined region over a complex terrain of Antarctica, including the Ross Ice Shelf and the Transantarctic Mountains. (e) Spatial distribution of grid size for V16km. (f) Spatial distribution of grid size for V4km.



Table 2. iAMAS configurations.

Basic parameter settings		Main physics options	
Parameter	Setting	Scheme	Option
Vertical levels	55	Convection	Grell-Freita (Grell and Freitas, 2014)
Initial condition	ERA5	Microphysics	Thompson (Thompson et al., 2008)
Each integration	5 days	Land surface	Noah (Tewari et al., 2016)
Spin-up time	24 h	Planetary boundary layer	MYNN (Nakanishi and Niino, 2006)
Output time interval	3 h	Longwave radiation	RRTMG (Iacono et al., 2008)
Period	Jan, Apr Jul, and Oct in 2015	Shortwave radiation	RRTMG (Iacono et al., 2008)

2.2 Data

2.2.1 ERA5

115 The ERA5 dataset, employed as the initial conditions for iAMAS in this study, is the fifth-generation ECMWF reanalysis
of global climate data (Hersbach et al., 2020). The motivation for using ERA5 to compare with iAMAS simulations is to
analyze whether biases in iAMAS are influenced by the initialized field or stem from the model itself, which is essential for
informing future model development. Additionally, the statistical results of ERA5 can serve as a reference for evaluating the
statistical performance of iAMAS. ERA5 integrates model data with global observations to produce a globally complete and
120 consistent dataset. In this study, both surface and upper atmospheric meteorological fields from ERA5 for January, April, July,
and October of 2015 will be analyzed. Surface data are derived from ERA5 hourly data at single levels with a resolution
of $0.25^\circ \times 0.25^\circ$ (<https://cds.climate.copernicus.eu/cdsapp#!/dataset/reanalysis-era5-single-levels?tab=overview>). This surface
data includes 2 m temperature, surface pressure, 2 m dewpoint temperature (for specific humidity calculation), and 10 m wind
speed. For upper atmospheric fields, ERA5 provides data at 37 pressure levels, also with a resolution of $0.25^\circ \times 0.25^\circ$ (<https://cds.climate.copernicus.eu/cdsapp#!/dataset/reanalysis-era5-pressure-levels?tab=overview>).
125 The profile data utilized in this study include geopotential height (for altitude calculation), temperature, relative humidity (for specific humidity calculation),
and wind speed.

This study analyzes specific humidity rather than relative humidity due to the high sensitivity of relative humidity calcu-
lations to temperature, particularly at typical low temperatures of Antarctica. The calculated relative humidity can exhibit
130 significant uncertainty in Antarctica. Therefore, this study utilizes specific humidity to describe the features of Antarctic water
vapor.

2.2.2 AWS

The surface layer measurements used to evaluate iAMAS simulations are obtained from the Antarctic Meteorological Re-
search Center (AMRC) and the Automatic Weather Station (AWS) program in Antarctica. During the model verification pe-



135 riod (January, April, July, and October of 2015), data from 55 AWS sites, recorded at 3-hour intervals, were available on the
AMRC website (<ftp://amrc.ssec.wisc.edu/pub/aws/q3h/2015>), although some records were incomplete. These AWS locations
are marked by the dots in Fig. 2. The AWS measurements underwent quality control using Interactive Data Language (IDL)
software (Lazzara et al., 2012). The height of the instrument for measuring meteorological parameters is nominally 3 m above
the snow surface; however, this distance varies with temporal changes in the snow surface due to accumulation.

140 In this study, we define a region referred to as RTM, which includes nearly all AWS stations (indicated by the 29 red dots
in Fig. 2) located on the Ross Ice Shelf and in the Transantarctic Mountains. Additionally, we designate a High Polar Plateau
(HPP) area, with an altitude exceeding 2.7 km (higher than the Henry AWS station at 2755 m at the South Pole), illustrated
by the area enclosed by the blue dashed line in East Antarctica (see Fig. 2). The AWS stations within the HPP are marked
by eight blue dots in Fig. 2. RTM is characterized by complex, low-altitude terrain, while HPP is a flat region at a relatively
145 high altitude, where strong surface temperature inversions have been observed (Yang et al., 2021a, b, 2023b, 2022). These two
regions exhibit distinct features, and their meteorological fields will be analyzed in detail later.

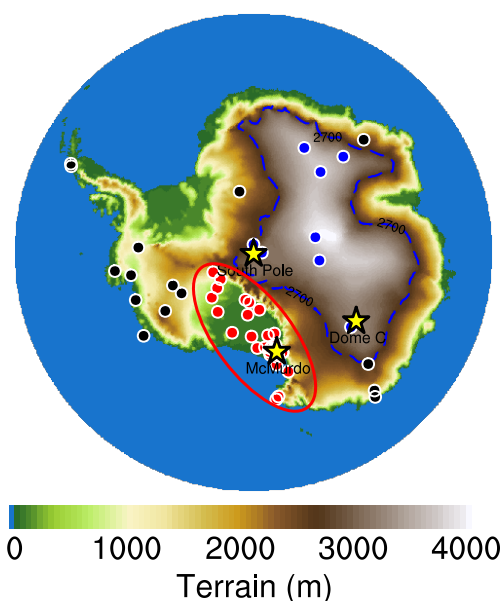


Figure 2. The elevation of the Antarctic continent and the adjacent ocean. The RTM region (including Ross Ice Shelf and Transantarctic Mountains) is delineated by a solid red line, while the HPP (High Polar Plateau) region is marked by a dashed blue line. Red and blue dots represent AWS locations within the RTM and HPP regions, respectively, whereas black dots indicate other AWS locations in Antarctica. The yellow stars with black edges denote the locations of McMurdo (78°S , 167°E), the South Pole (90°S , $\dots^{\circ}\text{E}$), and Dome C (75°S , 123°E), where sounding balloons were launched.



2.2.3 Radiosonde

This study utilizes radiosonde measurements from three representative sites on the Antarctic continent: McMurdo (MM) on the coast, the South Pole (SP) on the flank, and Dome C (DC) at the summit. MM is situated on Ross Island, near the Transantarctic Mountains, which feature relatively complex terrain (i.e., the RTM region). In contrast, SP and DC are located within the HPP region, characterized by relatively flat terrain. Daily radiosonde measurements at MM and SP are available from the AMRC (<ftp://amrc.ssec.wisc.edu/pub>), while measurements at DC are obtained from the Antarctic Meteo-Climatological Observatory (<http://www.climantartide.it>). The locations of these three radiosounding sites are marked by yellow stars in Fig. 2. The radiosonde measurements provide high-resolution profiles of temperature, pressure, relative humidity (which is used to calculate specific humidity), and wind speed. Radiosounding at MM and SP is conducted twice daily at 00:00 and 12:00 UTC, while at DC, it is launched once daily at 12:00 UTC. Some data are missing, likely due to the harsh Antarctic environment. In total, 182, 194, and 116 sounding profiles are available at MM, SP, and DC, respectively, for January, April, July, and October of 2015. It is important to note that MM, SP, and DC are all located within the 4-km grid resolution region of V4km in Fig. 1, allowing these radiosonde measurements to evaluate the impact of increasing iAMAS horizontal resolution to 4 km on enhancing simulations.

3 Results

3.1 Fields near the surface

The iAMAS surface-layer simulations over the Antarctic continent are evaluated by comparing them with ERA5 data and AWS measurements. The temperature, pressure, specific humidity, and wind speed within surface layer are analyzed. Surface-layer variables from iAMAS and ERA5 are compared using the nearest points to the latitude and longitude of each AWS location. For both iAMAS and ERA5, 2-m temperature and specific humidity are used for direct comparison, despite the AWS sensors being nominally positioned 3 m above the snow surface. However, maintaining the sensors at a fixed height is challenging due to snow accumulation at many sites (Lazzara et al., 2012). Surface pressure is corrected using the hypsometric equation to account for altitude differences between the model surface (iAMAS and ERA5) and the AWS locations. For wind speed, the 10-m wind speeds from both iAMAS and ERA5 are adjusted using the logarithmic wind profile down to 3 m above the model surface to correspond more closely to the AWS wind measurements.

3.1.1 2-m temperature

The seasonal variation of 2-m temperature for ERA5 is illustrated in the first column of Fig. 3. The temperature contour from ERA5 shows that January exhibits the highest 2-m temperature compared to the other three months. The black downward triangles over the HPP for January suggest an underestimation of 2-m temperature by ERA5. In the colder months of April and July, the upward white triangles within the HPP region indicate that ERA5 overestimates the 2-m temperature in the high interior. The temperature in October falls within the mid-range for the four months, with relatively small positive bias



in ERA5 temperature within the HPP region during this month. In summary, the statistics over the four months indicate an underestimation of high temperatures and an overestimation of low temperatures by ERA5 over the high Polar Plateau.

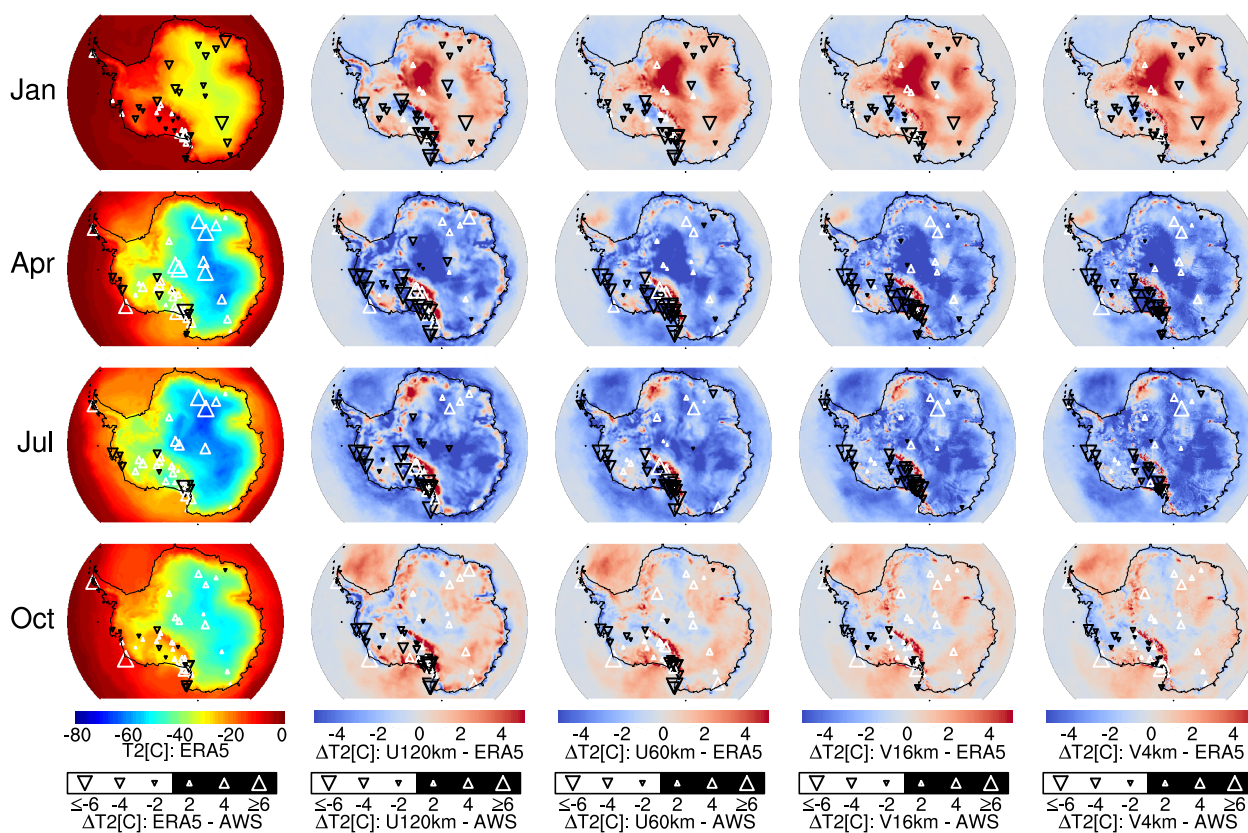


Figure 3. The first column displays the monthly median 2-m temperature ($T_2[^\circ\text{C}]$) for ERA5. The four rightmost columns show the monthly median values of 2-m temperature biases ($\Delta T_2[^\circ\text{C}]$) for iAMAS minus ERA5. The magnitudes of the monthly median biases for the model (ERA5 or iAMAS) minus AWS are indicated by the size of the overlaid triangles; black downward-pointing triangles represent negative biases, and white upward-pointing triangles represent positive biases.

180 Comparison of iAMAS with ERA5 in Fig. 3 reveals that all four iAMAS experiments at various resolutions generally simulate warmer temperatures than ERA5 in January, but show colder temperatures in April and July. In October, the simulated temperatures from iAMAS are closer to those of ERA5 than in the other three months. In particular, for April and July, the temperature simulated by the four iAMAS experiments at various resolutions all align more closely with AWS measurements than those from ERA5 within the HPP region. This is evidenced by the smaller sizes of the triangles indicating biases for iAMAS
 185 minus AWS compared to those for ERA5 (see April and July in Fig. 3). Fig. 4 provides an example from the South Pole over the HPP, suggesting that ERA5 overestimates cold temperatures in April and July, whereas iAMAS (regardless of the chosen resolution) better captures the temperature trends during the cooling process. Fréville et al. (2014) also identified a widespread



overestimation of temperature in ERA reanalysis data when compared to Moderate Resolution Imaging Spectroradiometer (MODIS) data in the Antarctic, they argue that this warm bias may result from an overestimation of surface turbulent fluxes under very stable conditions. Interestingly, we also found that the warm bias in ERA5 corresponds to meteorological situations characterized by temperature inversions, as the correlation coefficient between the temperature inversion and ERA5 warm bias reaches 0.49. This confirms that ERA5 demonstrates inaccurate temperature estimations under inversion conditions in Antarctica. While iAMAS does not exhibit the overestimation of stable stratification temperature observed in ERA5, suggesting that iAMAS more accurately represents the surface temperature of the Antarctic plateau than ERA5.

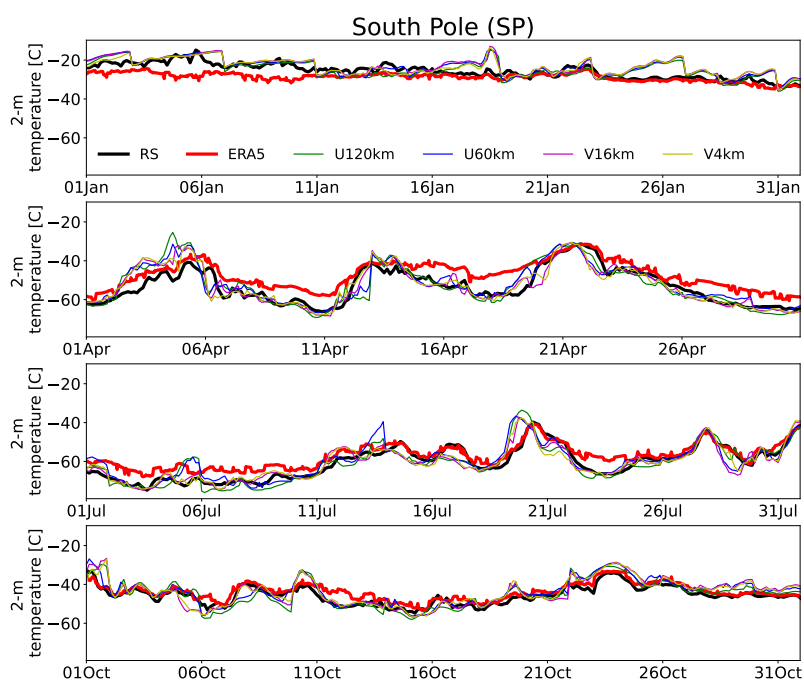


Figure 4. The time series of surface-layer temperatures at the South Pole for January, April, July, and October of 2016.

Table 3 presents the temperature statistics from the models (ERA5 and iAMAS) in comparison to AWS observations, including the Root Mean Square Error (RMSE) and median bias (BIAS; where $BIAS = \text{median}[\text{model} - \text{AWS}]$). The BIAS values for iAMAS temperature at various resolutions over the RTM region, as shown in Table 3, are all negative, indicating a cold bias over the Ross Ice Shelf. This finding is consistent with the simulation results from another model (regional atmospheric model CCLM; Zentek and Heinemann, 2020) applied to a similar environment (Filchner–Ronne Ice Shelf) in Antarctica. In the RTM region, both the U60km (RMSE: 4.16 to 7.66°C) and V16km (RMSE: 3.69 to 7.61°C) show no significant improvements and, in some cases, even performs slightly worse than the U120km (RMSE: 3.95 to 7.75°C). It is the V4km (RMSE: 3.16 to 6.63°C) demonstrates improvements in temperature simulations across all the four months.

In the HPP region, the magnitude of temperature biases for iAMAS at four resolutions are all smaller than that of ERA5 during April and July (see Table 3), indicating that iAMAS more accurately captures the cooling process during these months



Table 3. Monthly RMSE (BIAS in parentheses) of the 2-m temperature for ERA5 and iAMAS compared with AWS. The unit is °C.

Region (Month)	ERA5	U120km	U60km	V16km	V4km
RTM (Jan)	2.30 (-0.03)	3.95 (-1.58)	4.16 (-1.15)	3.69 (-0.61)	3.16 (-0.63)
RTM (Apr)	3.61 (1.60)	7.07 (-2.11)	7.66 (-2.97)	7.34 (-2.69)	6.16 (-2.33)
RTM (Jul)	3.81 (1.02)	7.75 (-0.66)	7.56 (-2.79)	7.61 (-2.61)	6.63 (-1.64)
RTM (Oct)	2.91 (0.60)	6.32 (-1.28)	6.20 (-0.82)	5.58 (-0.01)	5.12 (-0.03)
HPP (Jan)	3.62 (-1.76)	3.73 (-1.25)	3.71 (-1.20)	3.67 (-0.79)	3.64 (-1.04)
HPP (Apr)	6.11 (5.42)	4.29 (0.88)	4.39 (0.95)	4.80 (2.06)	4.41 (1.90)
HPP (Jul)	4.87 (3.39)	5.45 (0.02)	5.08 (0.07)	5.15 (1.54)	4.80 (1.16)
HPP (Oct)	3.16 (1.60)	4.18 (1.52)	3.97 (1.78)	4.05 (1.64)	3.81 (1.59)

205 (see the South Pole example within HPP in Fig. 4). Based on all four months statistics presented in Table 3, U120km, U60km, V16km, and V4km demonstrate overall reductions in temperature RMSE of 0.6%, 3.6%, 0.5%, and 6.6%, respectively, compared to ERA5. This suggests that iAMAS performs comparably to, and in some cases better than, ERA5 in representing 2-m temperature. On the other hand, when compared to U120km (RMSE: 3.73 to 5.45°C), U60km (RMSE: 3.71 to 5.08 °C) shows a moderate reduction in temperature errors across this flat terrain (i.e., HPP). However, further increases in horizontal
 210 resolution from U60km to V16km (or V4km) result in minimal reductions in temperature RMSE.

In summary, a grid resolution of 4 km or finer is recommended for iAMAS to simulate 2-m temperatures in complex terrain (i.e., RTM) in Antarctica, while a resolution of 60 km seems to be adequate for flat terrain (i.e., HPP).

3.1.2 Surface pressure

The evaluation of surface pressure is presented in Fig. 5. The four rightmost columns indicate that discrepancies between
 215 iAMAS and ERA5 decrease with increasing iAMAS grid resolution. The iAMAS pressure simulations exhibit positive biases over the escarpment region and negative biases along the coast, with these biases being more pronounced for U120km compared to ERA5. This discrepancy may be due the resolution of the iAMAS model spatially smooths the topography, resulting in mismatched elevations between iAMAS and ERA5 grid points. Since the elevation biases (iAMAS minus ERA5) are found to be negative over the escarpment region and positive along the coast (not shown).

220 When comparing iAMAS simulations with AWS measurements within the RTM region with complex terrain, the pressure biases for different grid resolutions all exhibit seasonal variations. Specifically, there is a smallest pressure bias in January (indicated by smaller triangles in Fig. 5) and a largest bias in July (indicated by larger triangles in Fig. 5) over the RTM region. In contrast, the HPP region does not show significant seasonal variations in pressure bias. Using Dome F (-77.31°S, 39.71°E) and Dome C as examples within the HPP, the biases at Dome F remain negative (-0.32 to -1.30 hPa) for each month, whereas
 225 Dome C consistently exhibits positive biases (2.36 to 3.79 hPa). Notably, the spatial distribution of iAMAS pressure biases at four grid resolutions over HPP closely resembles that of ERA5, suggesting that the surface pressure bias in iAMAS over the flat terrain (i.e., HPP) may be attributed to its initial condition (here is ERA5).

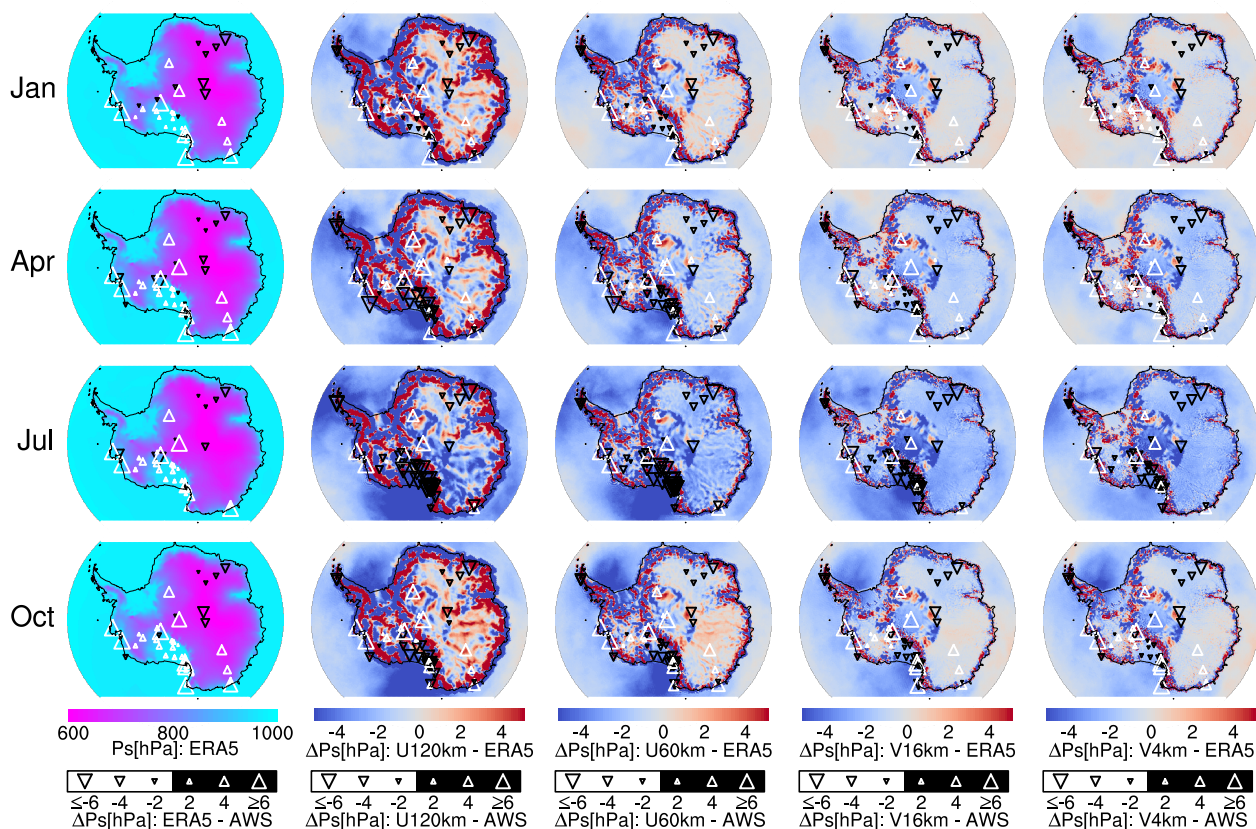


Figure 5. As Fig. 3 but for surface pressure (Ps[hPa]).

Table 4 presents the performance of iAMAS in reproducing surface pressure. In the RTM region, a finer resolution is essential, as the pressure RMSE decreases from U120km (RMSE: 2.41 to 8.29 hPa) to V4km (RMSE: 2.14 to 4.84 hPa). In

Table 4. Monthly RMSE (BIAS in parentheses) of the surface pressure for ERA5 and iAMAS compared with AWS. The unit is hPa.

Region (Month)	ERA5	U120km	U60km	V16km	V4km
RTM (Jan)	0.70 (0.44)	2.41 (-0.26)	2.74 (-0.29)	2.20 (0.01)	2.14 (0.43)
RTM (Apr)	1.12 (0.60)	6.42 (-2.50)	6.27 (-2.03)	4.11 (-0.84)	3.18 (-0.02)
RTM (Jul)	1.47 (0.82)	8.29 (-5.83)	7.32 (-5.03)	5.62 (-3.48)	4.84 (-2.29)
RTM (Oct)	1.39 (1.14)	5.28 (-2.69)	4.84 (-1.51)	4.15 (-1.38)	3.26 (-0.58)
HPP (Jan)	2.11 (-1.12)	2.60 (-1.21)	2.50 (-1.08)	2.59 (-1.16)	2.57 (-1.08)
HPP (Apr)	1.75 (-0.28)	3.44 (-0.09)	3.20 (0.00)	3.43 (-0.79)	3.01 (-1.49)
HPP (Jul)	0.96 (-0.27)	4.65 (-1.94)	4.19 (-2.10)	4.46 (-2.37)	4.37 (-2.45)
HPP (Oct)	2.03 (-0.45)	3.10 (-0.86)	3.05 (-1.10)	3.03 (-1.35)	3.13 (-1.28)



230 contrast, for the HPP, Table 4 indicates that a 60-km grid resolution is sufficient for iAMAS to simulate pressure, as further increases in grid resolution yield minimal improvements.

The RMSE and BIAS presented in Table 4 were calculated using adjusted pressure, applying the hypsometric relationship to reduce biases arising from height differences between the surface grids of the models (iAMAS and ERA5) and AWS sensors. This adjustment strategy has effectively reduced the pressure bias; for instance, the pressure RMSE of U120km within the
 235 RTM region in January is 20.48 hPa without using the hypsometric relationship, whereas the RMSE for adjusted pressure is only 2.41 hPa.

3.1.3 2-m specific humidity

Figure 6 illustrates the biases in 2-m specific humidity. In the HPP region, ERA5 predominantly exhibits wet biases throughout the year. In contrast, all four iAMAS experiments at various resolutions show clear seasonal variations over the HPP region.
 240 Dry biases are more pronounced during the warmer months of January and October, while wet biases become more prominent during the colder months of April and July.

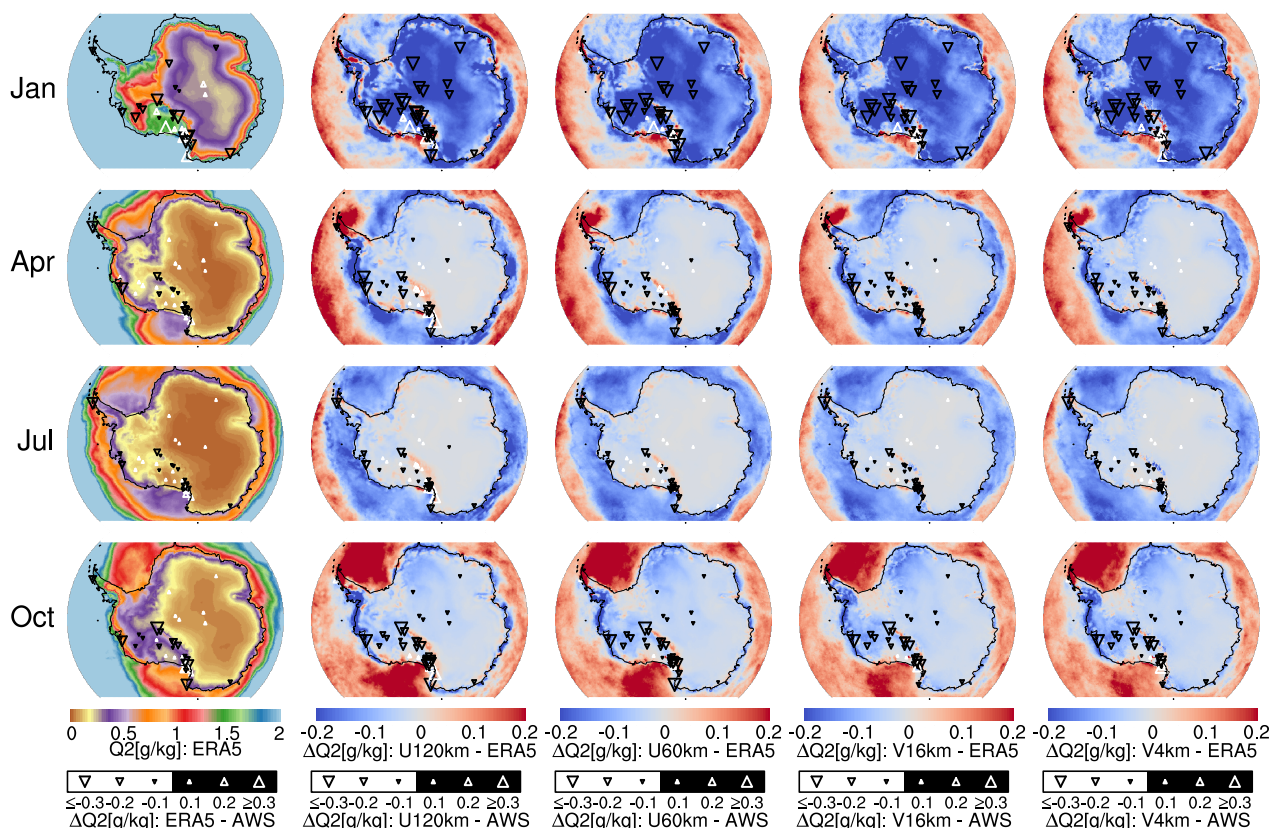


Figure 6. As Fig. 3 but for 2-m specific humidity (Q_2 [g/kg]).



Table 5. Monthly RMSE (BIAS in parentheses) of the 2-m specific humidity for ERA5 and iAMAS compared with AWS. The unit is g/kg.

Region (Month)	ERA5	U120km	U60km	V16km	V4km
RTM (Jan)	0.4133(-0.0267)	0.5786(-0.2404)	0.5470(-0.1992)	0.4961(-0.1381)	0.4601(-0.1007)
RTM (Apr)	0.1333(-0.0064)	0.1853(-0.0068)	0.1864(-0.0263)	0.1716(-0.0426)	0.1613(-0.0467)
RTM (Jul)	0.1081(-0.0047)	0.2242(-0.0009)	0.1768(-0.0226)	0.1724(-0.0310)	0.1681(-0.0148)
RTM (Oct)	0.1674(-0.0537)	0.3352(-0.1396)	0.3468(-0.1004)	0.2866(-0.0862)	0.2911(-0.0758)
HPP (Jan)	0.1051(-0.0054)	0.3148(-0.2346)	0.3368(-0.2350)	0.3067(-0.2188)	0.3090(-0.2292)
HPP (Apr)	0.0275(0.0216)	0.0306(0.0016)	0.0180(0.0017)	0.0154(0.0018)	0.0180(0.0027)
HPP (Jul)	0.0083(0.0053)	0.0211(0.0004)	0.0184(0.0011)	0.0151(0.0018)	0.0152(0.0016)
HPP (Oct)	0.0251(0.0142)	0.0482(-0.0250)	0.0442(-0.0221)	0.0491(-0.0213)	0.0468(-0.0200)

Table 5 presents the RMSE and BIAS for 2-m specific humidity. In the RTM region, iAMAS specific humidity values at various resolutions are all drier than those from AWS, e.g., BIAS values for U120km ranging from -0.0009 to -0.2404 g/kg. Similar dry biases were also noted in AMPS simulations (Wille et al., 2016), suggesting that this underestimation may arise from the Unified Noah Land Surface Model (also utilized by iAMAS in this study), which does not account for sublimation from blowing snow. Furthermore, the magnitudes of underestimation in iAMAS simulations at various resolutions are all greater during the warm months than in the cold months within the RTM region. Notably, increasing the grid resolution from U120km (RMSE: 0.1853 to 0.5786 g/kg) to V4km (RMSE: 0.1613 to 0.4601 g/kg) can reduce humidity errors over the RTM region. In the HPP region, increasing the iAMAS grid resolution does not significantly improve specific humidity simulations. Spatially, the RTM region, characterized by lower altitudes, has warmer air compared to the HPP; the iAMAS simulations exhibit more pronounced dry biases within the RTM than in the HPP. Temporally, dry biases are more significant during the warm months than in the cold months. In summary, iAMAS appears to underestimate specific humidity in warmer conditions.

3.1.4 3-m wind speed

Persistent katabatic winds are a distinctive meteorological phenomenon over the Antarctic plateau. This is demonstrated by the ERA5 3-m wind speed data in the first column of Fig. 7, which shows an increase in wind speed from the summit of the inland plateau to the escarpment region, where katabatic winds prevail over the escarpment region with steep surface (Parish and Casano, 2001; Ma et al., 2010; Rinke et al., 2012). Fig. 7 indicates that iAMAS at various resolutions all reproduce stronger wind speeds than ERA5 over complex terrain, particularly just inland from the coast and the Transantarctic Mountains. The iAMAS simulations with higher grid resolutions show a reduction in such positive wind bias. As grid resolution increases, iAMAS better resolves the complex terrain, enhancing the barrier effect of air flowing over it (similar to Argentini and Mastrantonio, 1994; O’connor and Bromwich, 1988), which subsequently leads to decreased wind speeds in iAMAS simulations. Similarly, Bromwich et al. (2005) compared the AMPS 10-km and 3.3-km resolution MM simulation domains and found that the higher resolution (3.3-km) domain provides a more accurate depiction of near-surface winds. They argued that the positive bias in wind speed is partly due to topographic smoothing.

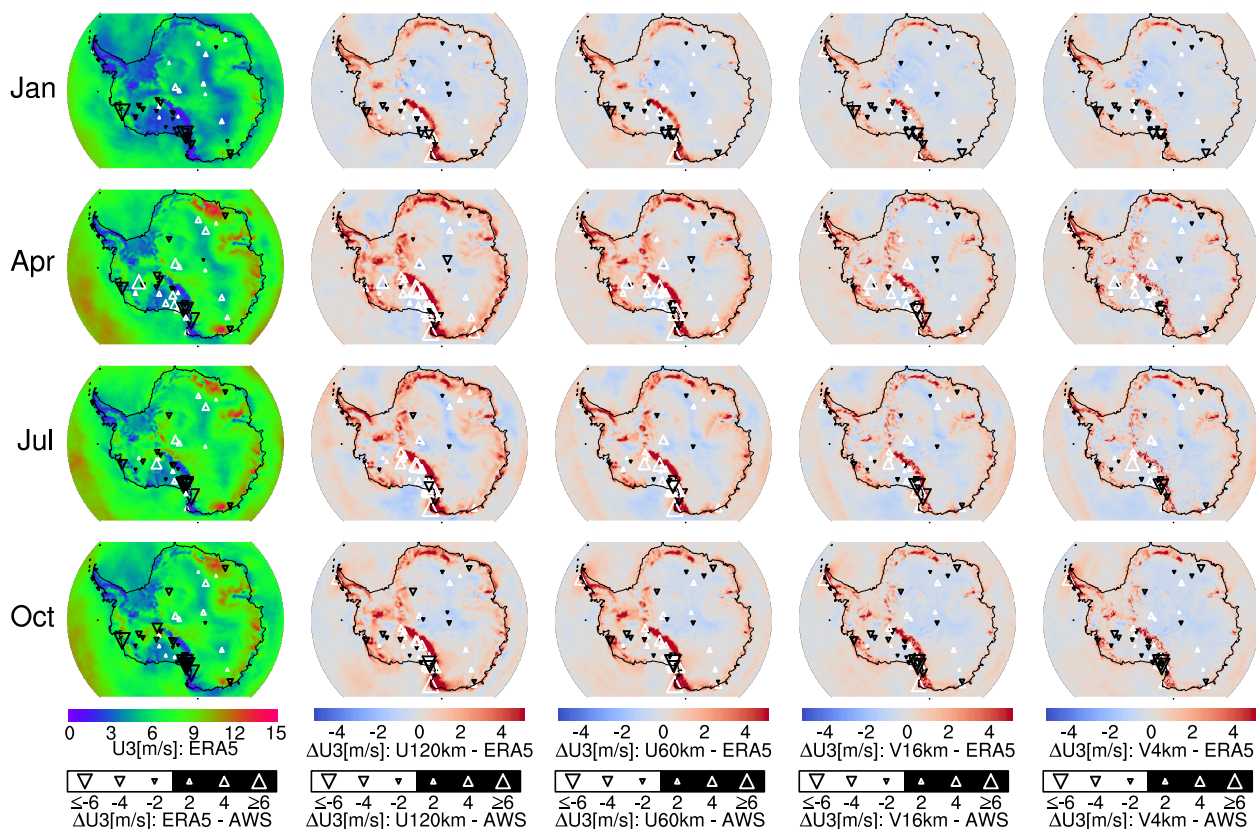


Figure 7. As Fig. 3 but for 3-m wind speed ($U3[m\ s^{-1}]$).

Table 6. Monthly RMSE (BIAS in parentheses) of the 3-m wind speed for ERA5 and iAMAS compared with AWS. The unit is $m\ s^{-1}$.

Region (Month)	ERA5	U120km	U60km	V16km	V4km
RTM (Jan)	1.98 (-0.55)	2.75 (0.33)	2.91 (0.02)	2.52 (-0.34)	2.53 (-0.35)
RTM (Apr)	2.87 (-0.28)	4.66 (2.24)	3.65 (1.54)	3.13 (0.70)	3.00 (0.68)
RTM (Jul)	3.13 (-0.63)	5.25 (2.61)	5.01 (0.86)	4.12 (0.25)	4.25 (0.13)
RTM (Oct)	2.85 (-0.84)	3.97 (2.08)	3.47 (0.30)	3.46 (-0.17)	3.00 (-0.25)
HPP (Jan)	1.26 (0.78)	1.59 (-0.03)	1.40 (0.18)	1.36 (0.41)	1.38 (0.38)
HPP (Apr)	1.90 (1.40)	2.05 (0.89)	1.89 (0.82)	1.91 (1.05)	1.77 (0.97)
HPP (Jul)	2.03 (1.30)	2.03 (0.59)	1.94 (0.12)	2.01 (0.79)	1.95 (0.58)
HPP (Oct)	1.52 (0.96)	1.98 (0.01)	1.96 (0.07)	2.01 (0.30)	1.93 (0.25)

265 In the context of complex terrain (i.e., RTM), Table 6 demonstrates that increasing the iAMAS grid resolution enhances wind speed simulations. The RMSE for wind speed has decreased from U120km (RMSE: 2.75 to 5.25 $m\ s^{-1}$) to V4km (RMSE: 2.53 to 4.25 $m\ s^{-1}$). Notably, U120km tends to overestimate wind speeds (BIAS: 0.33 to 2.61 $m\ s^{-1}$), whereas the high-resolution



iAMAS simulations (e.g., V4km with a BIAS of -0.35 to 0.68 m s^{-1}) indicate a smaller wind speed positive bias. As previously discussed, the barrier effect of mountains becomes more pronounced with a higher-resolution grid, leading to a decrease in wind speed.

Over the HPP with flat terrain, Table 6 shows that the performance of iAMAS wind speed simulations is comparable to ERA5. For example, the RMSE for U120km (RMSE: 1.59 to 2.05 m s^{-1}) is quite close to that of ERA5 (RMSE: 1.26 to 2.03 m s^{-1}). In such flat regions, there is little difference in the RMSE statistic between the four iAMAS experiments with different grid resolutions. Once again, the results suggest that enhancing model grid resolution over flat regions in Antarctica is not urgently necessary.

3.2 Upper atmospheric fields

The iAMAS simulations were evaluated against radiosonde measurements from three sites (MM, SP, and DC) to assess their performance in the upper atmosphere over the Antarctic continent. To ensure robust results, data corresponding to altitudes reached by radiosondes fewer than five times per month were excluded. ERA5 data, used as the initial conditions for iAMAS, were also utilized for site analyses of upper-air meteorological fields. Data from four months (January, April, July, and October 2015), consistent with the surface layer analyses (Section 3.1), were collected.

The extracted model results (iAMAS and ERA5) for comparison were derived from the nearest grid points to the balloon launch sites. Balloons drifted significantly (by tens of kilometers) due to stronger winds in the stratosphere, which may increase the distance between the model grid point and the balloon, causing potential meteorological deviations. However, the stratosphere is generally stable, and we found that the meteorological fields within this layer from iAMAS varied slightly between the balloon launch and explosion locations (not shown). In contrast, the troposphere, especially near the ground, is relatively unstable, leading to significant variability in meteorological fields over small spatial scales. Thus, using the nearest model grid to the ground-launching position may be more appropriate for analyzing the model's performance. Additionally, time differences greater than two hours between model data (ERA5 and iAMAS) and radiosonde measurements were excluded from the comparison. Both radiosonde measurements and ERA5 reanalysis data were linearly interpolated to the height of the iAMAS grid for each site.

3.2.1 Upper air temperature

The monthly median differences in temperature profiles between the models (ERA5 and iAMAS) and radiosonde measurements above ground level (AGL) are illustrated in Fig. 8. The absence of values in the upper atmosphere for July suggests that the radiosonde balloons do not ascend as high as in other months, likely due to the fragility of the balloon's elastic material in colder seasons, which makes them more prone to explosion (Hagelin et al., 2008).

Near the ground at MM, both U120km and U60km exhibit a clear tendency to increase negative bias very close to the surface, potentially resulting in more pronounced surface temperature inversions. Here, we defined the inversion intensity as the temperature gradient between the second grid (76.6 m) and the first grid (23.5 m) above ground level. The results for April indicate that U120km (22 K m^{-1}) exhibits stronger temperature inversions compared to radiosonde measurements (3 K m^{-1}).

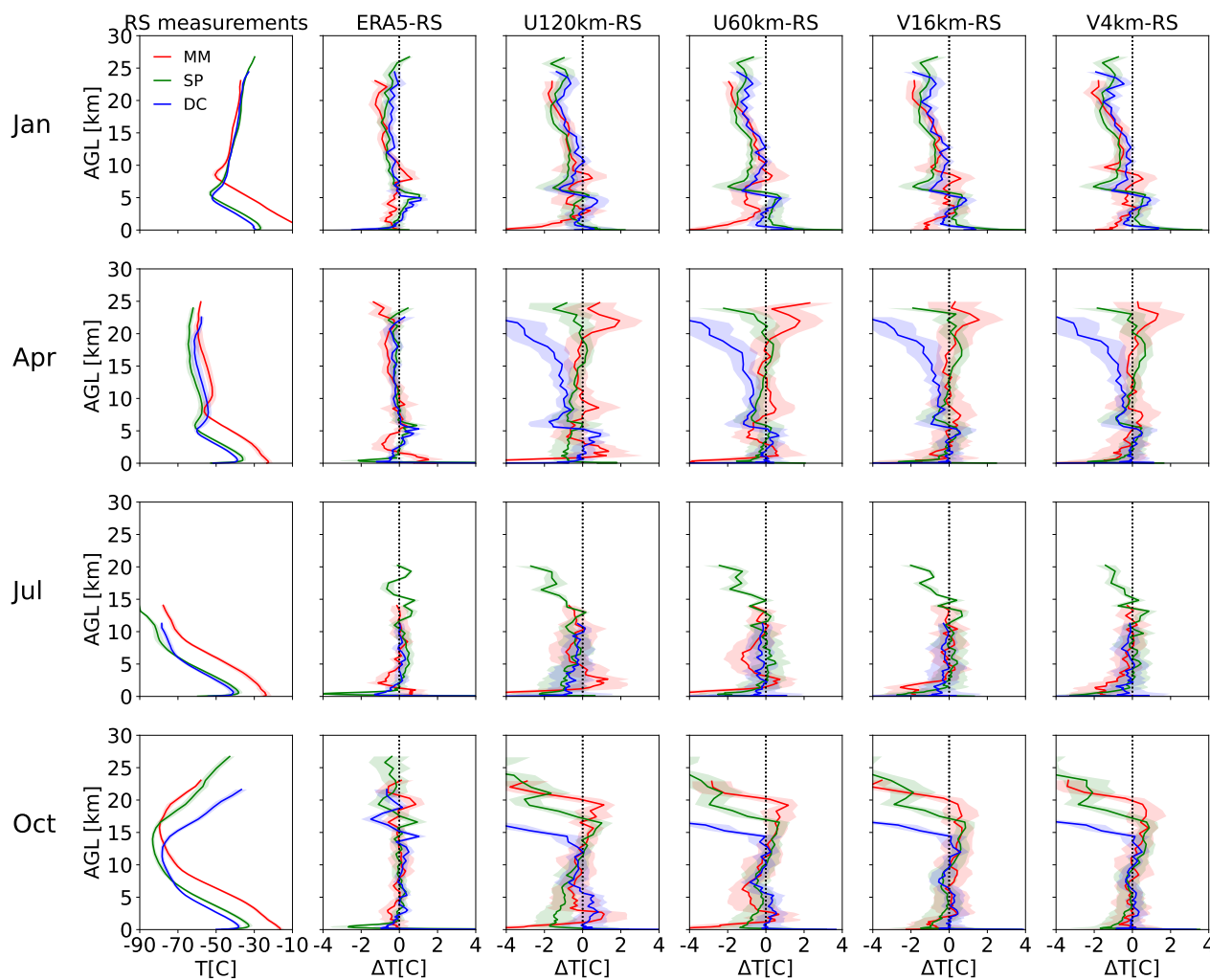


Figure 8. The first column displays the monthly medians of radiosonde-measured temperature (T [$^{\circ}\text{C}$]) profiles. The five rightmost columns present the monthly median temperature biases (ΔT [$^{\circ}\text{C}$]) for ERA5 and iAMAS (U120km, U60km, V16km, and V4km) compared to radiosonde measurements. The shading represents the standard error.

This model error, characterized by overestimated temperature inversions, was also observed in the AMPS simulations (Silber et al., 2019), which attributes this error to the model’s underestimation of surface downwelling longwave radiation. Encouragingly, a comparison of the rightmost four columns in Fig. 8 shows that increasing grid resolution can reduce the near-ground temperature bias at MM. Notably, significant temperature deviations have been observed at high altitudes in the iAMAS simulations, particularly in October with a cold bias exceeding 10°C at 20 km above ground level. These high-altitude temperature deviations have been identified across different grid resolutions. Additionally, significant cold biases at such altitudes during this period have also been reported in AMPS simulations (Yang et al., 2023a). This high-altitude temperature bias may be partly



due to the lack of radiosonde measurements, as extreme cold temperatures in Antarctica increase the likelihood of sounding balloons bursting. Consequently, model errors tend to increase in the absence of measurements constraints, as observed by ERA5, which also exhibits a tendency to produce larger temperature errors at high altitudes.

Figure 8 illustrates that discrepancies between iAMAS simulations with different grid resolutions primarily occur in the lower troposphere. Then, the temperature RMSE and BIAS for the 0-5 km altitude range are presented in Table 7. Additionally, temperature (plus pressure, specific humidity, and wind speed to be discussed later) statistics for the 5-15 km and 15-25 km ranges are included in the supplementary information for readers interested in high-altitude simulation performance. The statistics for the 5-15 km and 15-25 km ranges indicates iAMAS simulation performance is similar with different resolution meshes. The BIAS values in Table 7 for all iAMAS simulations with various resolutions at the MM site are negative, indicating a cold bias for each month in this coastal region, consistent with the surface-layer statistics (see RTM in Table 3). The V4km (RMSE: 1.55 to 3.41 °C) demonstrates a superior representation of temperature at the MM site compared to U120km (RMSE: 3.29 to 5.72 °C), highlighting the importance of increasing grid resolution in coastal areas.

Table 7. Monthly RMSE (BIAS in parentheses) of the 0-5 km temperature (°C) for ERA5 and iAMAS compared with radiosondes.

Site (Month)	ERA5	U120km	U60km	V16km	V4km
MM (Jan)	0.88 (-0.39)	3.29 (-1.36)	2.94 (-1.59)	1.72 (-0.69)	1.55 (-0.65)
MM (Apr)	1.77 (0.14)	5.16 (-0.53)	4.05 (-0.70)	3.49 (-0.39)	3.32 (-0.61)
MM (Jul)	1.62 (-0.07)	5.72 (-0.98)	4.62 (-1.16)	3.05 (-1.08)	3.41 (-1.06)
MM (Oct)	1.27 (-0.20)	4.63 (-0.81)	4.01 (-1.04)	2.72 (-0.32)	2.36 (-0.19)
SP (Jan)	1.05 (-0.01)	1.89 (-0.18)	2.20 (0.53)	2.25 (0.55)	2.16 (0.53)
SP (Apr)	3.48 (-0.01)	2.32 (-0.73)	2.42 (-0.23)	2.48 (-0.24)	2.46 (-0.20)
SP (Jul)	3.84 (0.00)	3.27 (-1.08)	2.82 (-0.47)	2.74 (-0.38)	2.62 (-0.38)
SP (Oct)	2.79 (-0.11)	2.73 (-1.13)	2.60 (-0.53)	2.57 (-0.38)	2.46 (-0.40)
DC (Jan)	1.39 (0.03)	1.77 (0.02)	1.74 (0.01)	1.79 (0.04)	1.81 (0.04)
DC (Apr)	2.26 (-0.05)	2.57 (0.06)	2.37 (0.09)	2.20 (-0.04)	2.27 (-0.03)
DC (Jul)	3.15 (-0.15)	3.81 (-0.80)	3.16 (-0.30)	3.20 (-0.45)	3.12 (-0.32)
DC (Oct)	2.05 (-0.04)	2.71 (0.41)	2.22 (0.27)	1.87 (0.13)	1.75 (0.12)

In the relatively flat region of central East Antarctica, which includes SP and DC, the representation of temperature at 0-5 km does not improve with higher-resolution iAMAS simulations across all months. For instance, in January, U60km (RMSE: 2.20 °C) performs slightly worse than U120km (RMSE: 1.89 °C) at SP, while in July, the temperature RMSE at SP moderately decreases from U120km (RMSE: 3.27 °C) to U60km (RMSE: 2.82 °C). Overall, there is little difference in the simulation results across the various iAMAS resolutions in these flat regions. It is noteworthy that during the colder months (April and October), the performance of iAMAS simulations can be comparable to, and occasionally better than ERA5 at SP and DC. For example, in April, the temperature RMSE for U120km is 2.32 °C at SP, which is lower than that of ERA5 (RMSE: 3.48 °C).



Overall, the temperature profile statistics exhibit a performance similar to those of the surface layer evaluation (Sect. 3.1.1), indicating that high-resolution grids for iAMAS should be employed in complex terrain. On the other hand, the V4km configuration incorporates regional mesh refinement over RTM, as opposed to the broader refinement applied across the entire Antarctic continent in the V16km configuration. Notably, V4km (last column in Table 7) performs better than V16km (second to last column in Table 7), suggesting that variable-resolution refinement should specifically focus on complex terrain to optimize computational efficiency.

3.2.2 Upper air pressure

Figure 9 illustrates the statistical analysis of pressure biases. ERA5 displays a positive pressure deviation at all three sites, with a particularly notable deviation at the DC site.

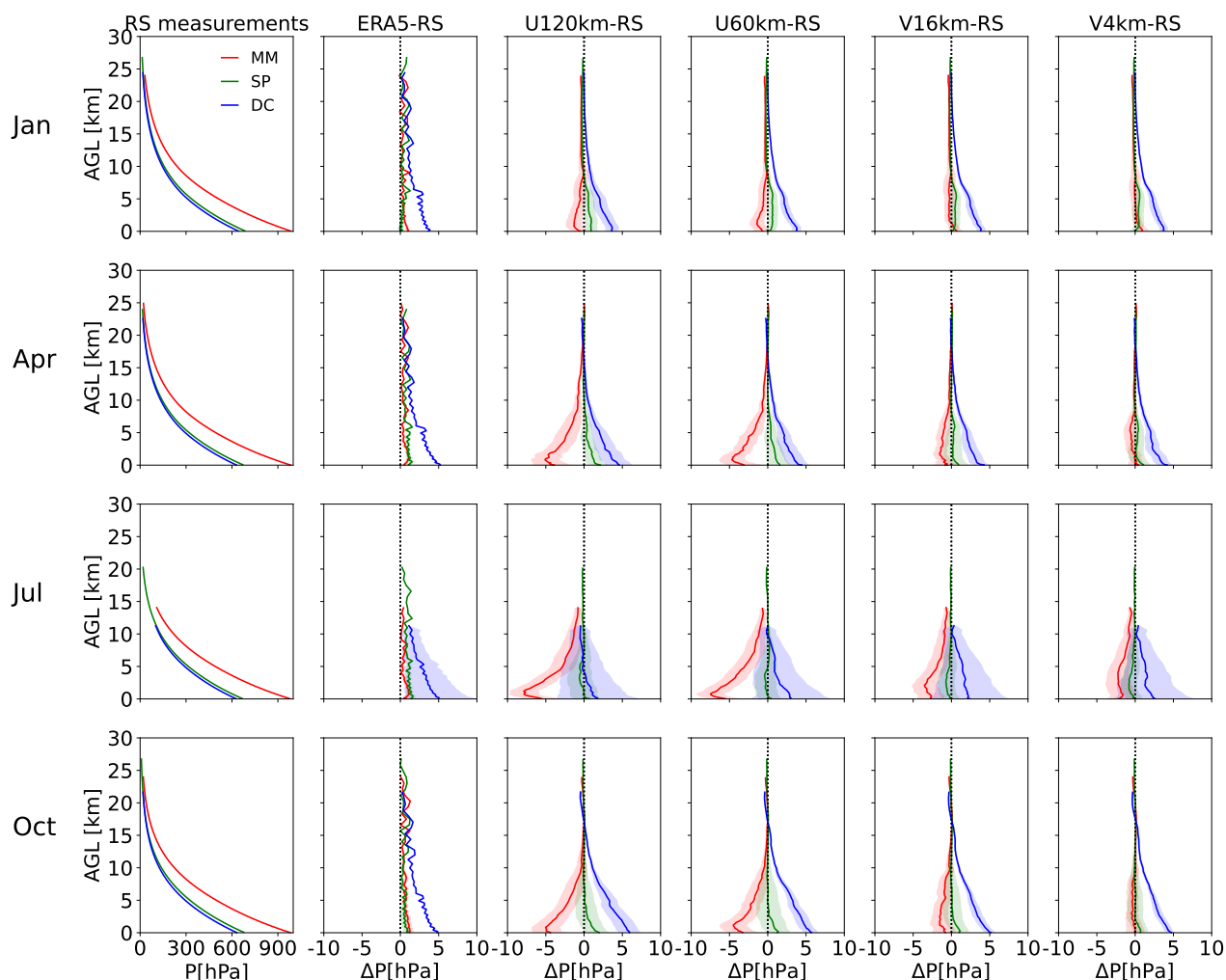


Figure 9. As Fig. 8 but for pressure (P[hPa]) profile.



Table 8. Monthly RMSE (BIAS in parentheses) of the 0-5 km pressure (hPa) for ERA5 and iAMAS compared with radiosondes.

Site (Month)	ERA5	U120km	U60km	V16km	V4km
MM (Jan)	0.81 (0.63)	2.30 (-0.97)	2.16 (-0.98)	1.42 (-0.06)	1.45 (0.38)
MM (Apr)	0.95 (0.71)	5.81 (-3.94)	5.04 (-3.46)	2.44 (-1.12)	1.86 (-0.26)
MM (Jul)	1.08 (0.75)	7.78 (-5.90)	7.15 (-5.29)	4.79 (-2.78)	4.15 (-2.11)
MM (Oct)	1.34 (0.98)	5.47 (-3.73)	5.27 (-3.36)	3.06 (-1.25)	2.11 (-0.16)
SP (Jan)	0.63 (0.20)	2.02 (0.80)	1.59 (0.54)	1.45 (0.43)	1.48 (0.40)
SP (Apr)	1.36 (1.13)	2.45 (1.06)	2.64 (0.96)	2.48 (0.33)	2.12 (0.42)
SP (Jul)	1.43 (1.23)	3.52 (-0.25)	2.90 (-0.13)	2.40 (-0.50)	2.29 (-0.52)
SP (Oct)	1.23 (0.66)	3.08 (0.90)	3.36 (0.71)	2.49 (0.56)	2.07 (0.32)
DC (Jan)	3.18 (3.10)	4.08 (3.19)	3.61 (3.14)	3.69 (3.21)	3.61 (3.14)
DC (Apr)	4.13 (3.97)	5.12 (3.29)	4.28 (3.09)	3.66 (2.92)	3.80 (2.96)
DC (Jul)	7.61 (3.91)	8.33 (0.63)	7.95 (2.12)	8.11 (1.84)	8.00 (1.81)
DC (Oct)	3.95 (3.81)	5.84 (4.71)	5.00 (4.52)	4.25 (3.88)	3.97 (3.72)

The discrepancies between all iAMAS simulations at various resolutions and radiosonde measurements exhibit minimal seasonal variation; the pressure biases at MM are consistently negative across all months, while the biases at DC are predominantly positive. The pressure bias at MM has significantly decreased from U120km to V4km (refer to the four rightmost columns of Fig. 9). This improvement is likely because high-resolution iAMAS can resolve terrain height more accurately, thus providing a better representation of pressure, as atmospheric pressure is strongly related to altitude. We observed that the actual altitude for launching the balloon at MM is 10 m. The model surface elevation of V4km (2 m) is considerably closer to the terrain height of MM compared to U120km (110 m; significant overestimation); thus, V4km yields a more accurate pressure profile.

To align with the height range of temperature statistics (Section 3.2.1), pressure errors within the 0–5 km altitude range have also been calculated, as detailed in Table 8. The pressure RMSE over complex terrain (i.e., MM) exhibits a substantial reduction from U120km (RMSE: 2.30 to 7.78 hPa) to V4km (RMSE: 1.45 to 4.15 hPa). As noted previously, U120km significantly overestimates the terrain height at MM; atmospheric pressure typically decreases with increasing altitude, which accounts for the negative pressure bias in U120km simulations at MM (BIAS: -0.97 to -5.90 hPa) shown in Table 8. In contrast, for SP and DC over flat regions, the increase in grid resolution for iAMAS does not result in a significant decrease in pressure RMSE as observed at the MM site. This is because the accuracy of terrain height over the flat region can be satisfactorily resolved by iAMAS even with a coarse mesh.

3.2.3 Upper air specific humidity

Figure 10 demonstrates that the specific humidity bias curve for all iAMAS experiments at various resolutions closely resembles that of ERA5. Therefore, the specific humidity bias in the upper air for iAMAS may be partly attributed to its initial conditions generated by ERA5. Comparisons of iAMAS simulations across different grid resolutions (see the four rightmost



355 columns in Fig. 10) indicate that the specific humidity bias profile at MM has been more significantly influenced by grid resolution, while the shape of the bias profile at SP and DC shows minimal sensitivity to horizontal resolution. It seems that grid resolution has a negligible impact on specific humidity over the flat regions represented by SP and DC, which is similar to surface-layer specific humidity analyses (Section 3.1.3).

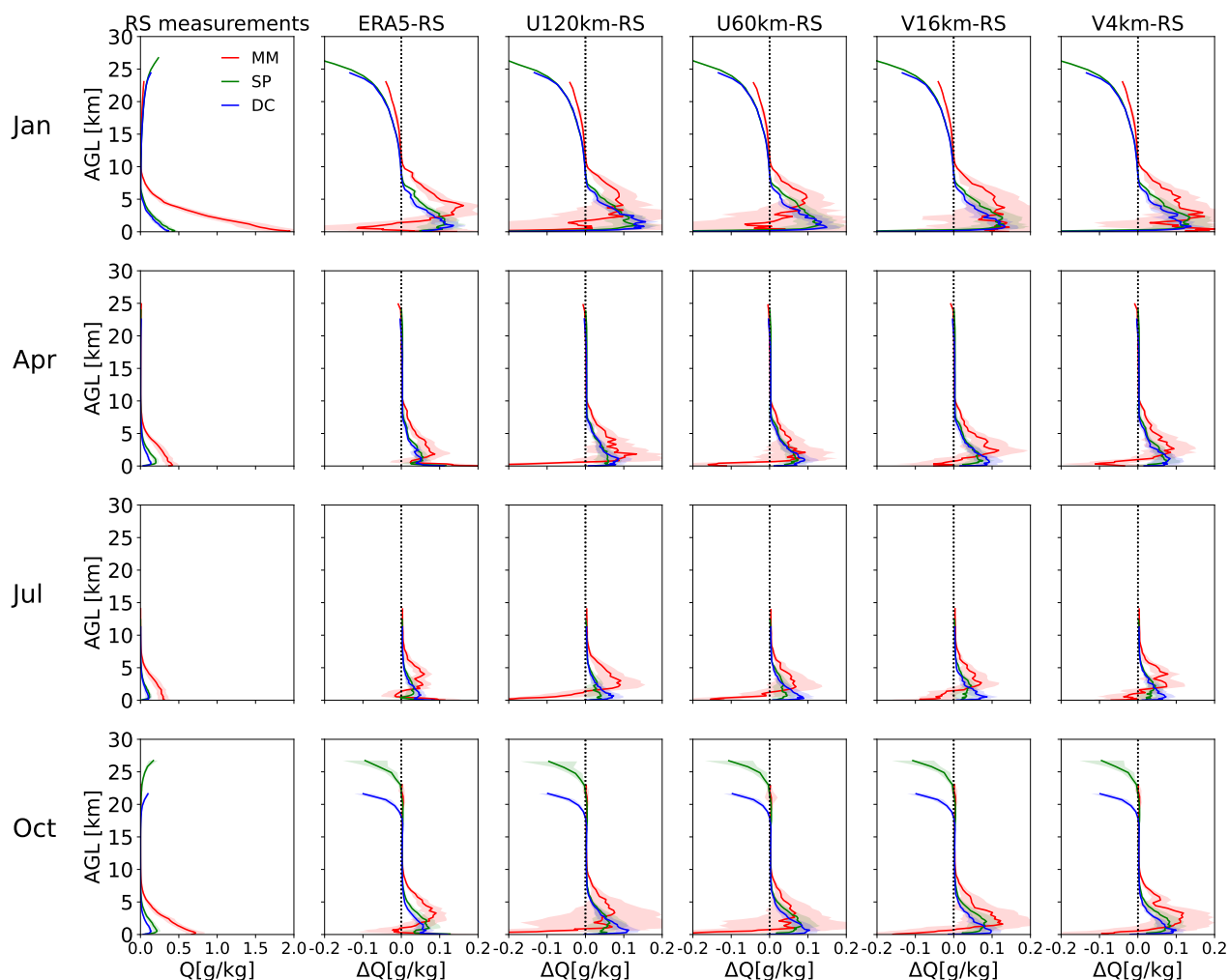


Figure 10. As Fig. 8 but for specific humidity (Q [g/kg]) profile.

360 Table 9 summarizes the statistics on RMSE and BIAS derived from specific humidity measurements within the 0–5 km altitude range. ERA5 generally overestimates specific humidity, with BIAS values at the three sites varying from 0.0212 to 0.0839 g/kg. All four iAMAS experiments at various resolutions overestimate specific humidity. Comparison of iAMAS simulations at different resolutions presented in Table 9 reveals that specific humidity simulations at MM, which features complex terrain, improve with finer iAMAS grid resolution, as RMSE decreases from U120km (RMSE: 0.1784 to 0.4625



Table 9. Monthly RMSE (BIAS in parentheses) of the 0-5 km specific humidity (g/kg) for ERA5 and iAMAS compared with radiosondes.

Site (Month)	ERA5	U120km	U60km	V16km	V4km
MM (Jan)	0.2899 (0.0838)	0.4625 (0.0209)	0.4532 (0.0370)	0.3373 (0.1080)	0.3558 (0.1268)
MM (Apr)	0.1220 (0.0645)	0.2214 (0.0244)	0.1864 (0.0169)	0.1632 (0.0457)	0.1554 (0.0354)
MM (Jul)	0.0931 (0.0387)	0.1784 (0.0163)	0.1485 (0.0055)	0.1083 (0.0144)	0.1215 (0.0301)
MM (Oct)	0.1390 (0.0556)	0.3714 (0.0114)	0.3163 (0.0179)	0.2391 (0.0461)	0.2338 (0.0601)
SP (Jan)	0.1213 (0.0838)	0.1618 (0.0746)	0.1781 (0.0780)	0.1781 (0.0825)	0.1797 (0.0867)
SP (Apr)	0.0608 (0.0404)	0.0671 (0.0431)	0.0720 (0.0454)	0.0707 (0.0437)	0.0733 (0.0464)
SP (Jul)	0.0430 (0.0212)	0.0574 (0.0230)	0.0565 (0.0276)	0.0568 (0.0282)	0.0565 (0.0297)
SP (Oct)	0.0739 (0.0483)	0.0827 (0.0386)	0.0910 (0.0520)	0.0914 (0.0565)	0.0907 (0.0559)
DC (Jan)	0.1113 (0.0825)	0.1387 (0.0867)	0.1421 (0.0821)	0.1399 (0.0794)	0.1361 (0.0775)
DC (Apr)	0.0575 (0.0372)	0.0799 (0.0496)	0.0854 (0.0544)	0.0859 (0.0550)	0.0859 (0.0477)
DC (Jul)	0.0482 (0.0280)	0.0635 (0.0295)	0.0692 (0.0377)	0.0624 (0.0313)	0.0620 (0.0347)
DC (Oct)	0.0614 (0.0401)	0.0902 (0.0573)	0.0841 (0.0566)	0.0759 (0.0474)	0.0731 (0.0477)

g/kg) to V4km (RMSE: 0.1215 to 0.3558 g/kg). However, in flat regions (i.e., SP and DC), specific humidity RMSE shows negligible reduction with finer iAMAS grid resolution.

In summary, high-resolution grids enhance simulation accuracy for specific humidity profiles in complex terrain but do not significant in flat terrain.

3.2.4 Upper air wind speed

Initially, ERA5 data at SP were extracted from a latitude of 90°S. We found that ERA5 wind speeds are significantly lower than radiosonde measurements (see red circles in Fig. 11). This discrepancy suggests that the ERA5 data may be affected by polar singularity issues, possibly due to the limitations of vector interpolation at the polar grid center (to be discussed later). Subsequently, data from grid points at a latitude of 89.75°S were obtained. We found that the ERA5 wind speeds at 89.75°S are reasonable and do not exhibit the significant underestimation of wind speed, as indicated by the blue crosses in Fig. 11.

Concerning the 3-m wind speed (Sect. 3.1.4), the ERA5 data at SP do not exhibit significant underestimation when compared to AWS measurements. This is because the two AWS sites (HEN: 89.02°S, 1.03°W; NIC: 89.00°S, 89.67°W) at SP are not located exactly at the polar grid center (90°S), thereby avoiding the polar singularity problem. Furthermore, the analysis of ERA5 surface-layer (10-m) wind speeds at a latitude of 90°S also indicates significant underestimation (not shown), consistent with the polar singularity issues identified in upper-air wind of ERA5 data.

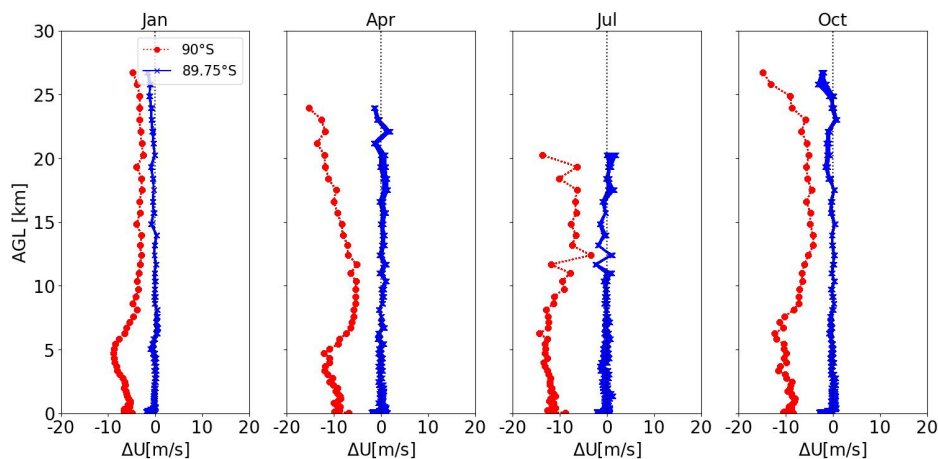


Figure 11. Monthly median values of wind speed biases (ΔU [m/s]) for ERA5 minus radiosondes. Red dots and blue crosses represent the results for 90°S and 89.75°S , respectively. Data are displayed for all longitudes (180°W to 180°E) at both 90°S and 89.75°S . The data for each longitude at 90°S are identical with overlapped points. While the results at 89.75°S exhibit slight differences across longitudes.

Given that the ERA5 wind speed at a latitude of 90°S appears less reliable, then the wind speed at the ERA5 grid point with coordinates 89.75°S , 0°E is utilized. The biases for the wind speed profile are displayed in Fig. 12. The wind speed bias for ERA5 is generally below 1 m s^{-1} in a large part of the atmosphere (see the second column in Fig. 12). The wind speed simulated by all four iAMAS experiments with various resolutions at SP seems unaffected by the ERA5 initialized field at 90°S and yield generally reasonable results. This may be attributed to the limited influence of a single grid point (i.e., the point at 90°S , 0°E) on the iAMAS simulations.

Interestingly, we found that the iAMAS simulations can replicate the unrealistically low wind speed values at 90°S after interpolating the iAMAS unstructured mesh to a regular latitude-longitude grid using the Earth System Modeling Framework (ESMF Balaji et al., 2024). Similarly, the ERA5 latitude-longitude grid data are interpolated from a Gaussian grid (Hersbach et al., 2020; Hortal and Simmons, 1991). We argue that the interpolation algorithm for ERA5 wind speeds (specifically, the U- and V-components) is unreliable at the polar grid center at 90°S , as the definition of wind direction becomes inapplicable here. In contrast to wind vectors, scalar quantities do not encounter this directional issue, which explains why temperature, pressure, and specific humidity in ERA5 do not exhibit this polar singularity problems.

Near the surface, iAMAS (specifically with coarse grid resolution, e.g., U120km) tends to simulate stronger wind speeds at MM. MM is located within the RTM region, this positive bias in wind speed over such complex terrain is consistent with the surface-layer analyses (Section 3.1.4). In the stratosphere, larger wind speed deviations have been observed in the iAMAS simulations across different grid resolutions, particularly in April, July, and October. Similar to the upper-air temperature (Section 3.2.1), this high-altitude wind speed bias may also be partly due to the lack of radiosonde measurements for model constraints.

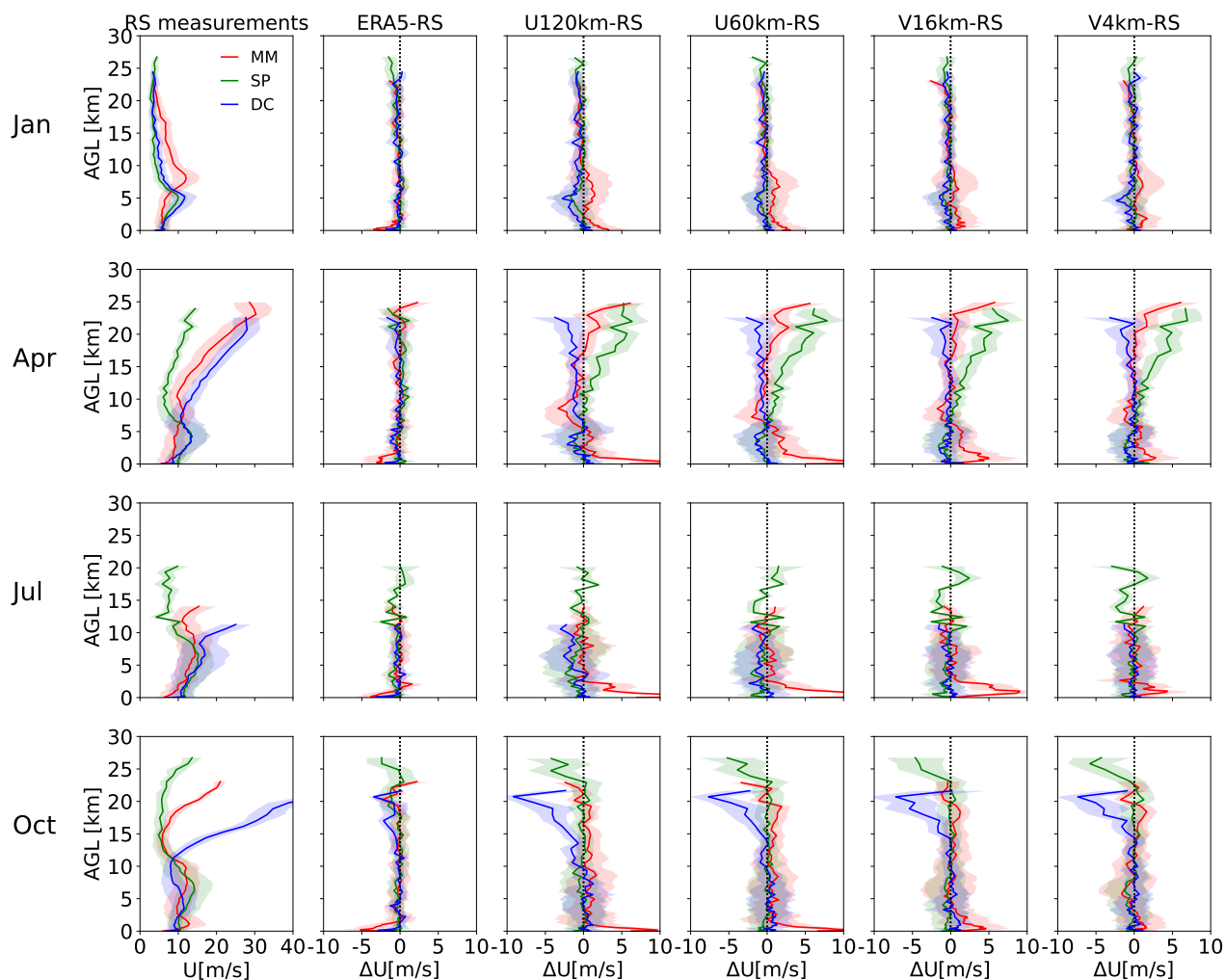


Figure 12. As Fig. 8 but for wind speed ($U[\text{m s}^{-1}]$) profile.

Table 10 demonstrates that the RMSE of wind speed in the 0-5 km range at MM is decreased from U120km (RMSE: 4.30 to 8.12 m s^{-1}) to V4km (RMSE: 4.00 to 5.39 m s^{-1}). This improvement can be attributed primarily to the more representative topography of the 4-km domain, as further evidenced by the comparison of 3-m wind speed simulations with AWS measurements over RTM (Sect. 3.1.4). For DC and SP in the flat HPP region, Table 10 indicates that the RMSE of wind speed simulations shows only minor variations across different iAMAS grid resolutions. For instance, at SP, U60km (RMSE: 3.05 to 5.10 m s^{-1}) exhibits slight improvements over U120km (RMSE: 3.25 to 5.43 m s^{-1}), while employing the computationally intensive V4km (RMSE: 2.72 to 4.32 m s^{-1}) does not significantly decrease the wind speed RMSE.



Table 10. Monthly RMSE (BIAS in parentheses) of the 0-5 km wind speed (m s^{-1}) for ERA5 and iAMAS compared with radiosondes.

Site (Month)	ERA5	U120km	U60km	V16km	V4km
MM (Jan)	2.90 (-0.73)	4.30 (1.02)	4.53 (1.25)	4.39 (0.49)	4.00 (0.33)
MM (Apr)	4.09 (-1.38)	7.78 (2.61)	8.97 (4.12)	6.11 (1.73)	4.94 (1.03)
MM (Jul)	3.94 (-0.95)	8.12 (4.33)	9.89 (5.38)	7.09 (2.63)	5.50 (0.88)
MM (Oct)	4.63 (-1.17)	8.02 (2.73)	8.16 (2.91)	6.47 (1.72)	5.39 (0.52)
SP (Jan)	1.78 (-0.21)	3.25 (-0.28)	3.05 (-0.21)	2.71 (-0.27)	2.72 (-0.17)
SP (Apr)	2.15 (-0.21)	4.22 (-0.17)	4.42 (-0.37)	4.10 (-0.54)	3.97 (-0.55)
SP (Jul)	2.15 (-0.69)	5.43 (-1.04)	5.10 (-0.98)	4.63 (-0.81)	4.32 (-0.45)
SP (Oct)	2.09 (-0.38)	4.63 (-0.07)	4.25 (-0.41)	4.37 (-0.48)	4.32 (-0.50)
DC (Jan)	1.59 (-0.36)	3.22 (-0.43)	2.53 (-0.25)	2.70 (-0.22)	2.69 (-0.26)
DC (Apr)	1.74 (-0.53)	4.68 (-0.06)	4.05 (-0.30)	4.00 (-0.40)	4.28 (-0.38)
DC (Jul)	2.29 (-0.34)	4.87 (-0.29)	5.19 (-0.31)	4.20 (0.10)	4.39 (-0.04)
DC (Oct)	2.05 (-0.46)	4.52 (0.36)	4.84 (0.66)	3.79 (0.66)	3.67 (-0.10)

405 4 Conclusions and discussions

Measurements from AWS and radiosondes collected on the Antarctic continent have been employed to assess the performance of an atmospheric model utilizing an unstructured mesh. The atmospheric model used in this study is the iAMAS model, which is equipped with various global mesh configurations (U120km, U60km, V16km, and V4km). Additionally, ERA5 data, serving as initial conditions for the iAMAS model, are included for comparative purposes. This study evaluates the performance of the iAMAS model concerning four routine meteorological fields: temperature, pressure, specific humidity, and wind speed from both the surface layer and the upper air. To our knowledge, this is the first instance of an explicit evaluation of a global unstructured mesh over the Antarctic, as previous studies of Antarctic simulations have predominantly utilized regional model with regular latitude-longitude grids.

A series of iAMAS simulations with lead times ranging from 2 to 5 days were combined to create a continuous time series for January, April, July, and October of 2015, allowing for an investigation of the seasonal characteristics of simulation bias. Two distinct regions, HPP with flat terrain and RTM with complex terrain, were emphatically analyzed. Performance statistics, including RMSE and BIAS, were demonstrated, and the underlying causes of model errors were investigated. Possible ways to remedy the simulation errors were discussed.

Regarding the surface layer within the RTM region characterized by complex terrain, the simulation capabilities of the iAMAS model for surface meteorological fields (2-m temperature, surface pressure, 2-m specific humidity, and 3-m wind speed) demonstrate improvements as the grid resolution increases from coarse (120 km) to fine (4 km). This trend indicates the necessity of higher grid resolution for accurately representing the complex topography in Antarctica. Notably, the simulated 2-m temperature from the U60km and V16km configurations shows no significant improvement and, in some instances, even worsens compared to U120km. While V4km shows improvements. This suggests that a grid resolution of 4 km, or finer, is



425 required over complex terrain. All four experiments conducted at various resolutions indicate cold biases at 2 m over RTM, such
cold biases were also found in other Antarctic simulations using regional models (e.g., CCLM: Zentek and Heinemann, 2020;
AMPS: Silber et al., 2019). Additionally, surface pressures are generally underestimated by the coarser resolution simulations
(i.e., U120km and U60km) over RTM, partly due to an overestimation of terrain height. All four iAMAS experiments at various
resolutions exhibits an overall dry bias when compared to specific humidity measurements taken by AWS in the RTM region.
430 For 3-m wind speed, positive biases have decreased from U120km to V4km, likely because the high-resolution grid more
effectively resolves the complex terrain, making the barrier effect of air passing over the terrain more pronounced and thus
reducing wind speed. The overestimated surface wind speeds over this region were also found in AMPS (Bromwich et al.,
2005).

In the surface layer over the flat region (i.e., HPP), the performance of iAMAS simulations varies only slightly across
435 different grid resolutions. A grid resolution of 60 km seems to be sufficient, as further increases in resolution yield negligible
improvements. Notably, all iAMAS experiments at four resolutions demonstrate comparable or even superior performance
in simulating temperature and wind speed relative to ERA5. The spatial distribution of iAMAS pressure biases over HPP
resembles that of ERA5, suggesting that the surface pressure bias in iAMAS over flat terrain may be attributed to its initial
conditions (i.e., ERA5). Regarding specific humidity at 2 m, iAMAS tends to underestimate humidity in warmer conditions,
440 particularly at low altitudes and during warm months.

In the upper air at MM within the RTM, the results again highlight the importance of increasing grid resolution over this
complex terrain. It was found that higher grid resolutions can reduce iAMAS biases in temperature, pressure, specific humidity,
and wind speed at MM. The U120km and U60km resolutions exhibit a notable tendency to increase negative bias in close
proximity to the ground, consistent with the previously observed cold bias in the surface layer, which may lead to more
445 pronounced surface temperature inversions. Regarding pressure bias, both U120km and U60km display a significant negative
bias at MM, partly due to an overestimation of terrain height. All four iAMAS experiments at various resolutions generally
overestimate specific humidity within the troposphere. Near the ground, U120km and U60km generate stronger wind speeds,
whereas V16km and V4km provide an enhanced depiction of winds.

Given the upper air results for SP and DC over the HPP region, it is not surprising that the discrepancies in iAMAS be-
450 tween different grid resolutions are minimal, similar to the surface-layer statistics observed in such a flat region. Notably, all
iAMAS simulations across various resolutions demonstrate comparable performance relative to ERA5 in temperature pro-
file simulations. As for pressure, the iAMAS model tends to overestimate pressure at the summit (i.e., DC) of the Antarctic
plateau. Analysis of specific humidity bias statistics reveals that all four iAMAS simulations at various resolutions are wetter
than radiosonde measurements within the troposphere. At the polar grid center (i.e., SP), ERA5 data at 90°S exhibit a polar
455 singularity issue, characterized by abnormally low wind speed values. This phenomenon may result from the inapplicability of
vector interpolation at the polar grid center, whereas scalar variables such as temperature, pressure, and specific humidity do
not experience this interpolation issue. The iAMAS wind speed simulations at SP appear unaffected by the ERA5 underesti-
mation at 90°S and yield overall reasonable results, likely because the bias at a single ERA5 point has limited influence on the
iAMAS simulation.



460 Overall, this study offers insights into the capability of the iAMAS model to capture meteorological characteristics in Antarc-
tica, identifying its limitations and proposing potential improvements for atmospheric modeling with unstructured meshes in
polar regions. Interestingly, the iAMAS does not show the polar singularity issue as in ERA5, that ERA5 exhibits significantly
underestimating the wind speeds at the polar grid center (i.e., the South Pole at the latitude of 90°S). Furthermore, all four
iAMAS experiments at various resolutions demonstrate comparable, and in some cases even superior, performance to ERA5
465 in terms of temperature and wind speed in the surface layer across the relatively flat regions of East Antarctica. The iAMAS
experiments in complex terrains (near the Transantarctic Mountains) indicate that refined meshes effectively enhance the simu-
lation of temperature, pressure, specific humidity, and wind speed for both the surface layer and the upper atmosphere. In such
complex terrain, grid resolutions of 4 km or finer are recommended. Conversely, for flat regions like the high East Antarctic
plateau, a grid resolution of 60 km appears to be adequate.

470 *Code availability.* The current version of the iAMAS model is available from the website: <https://doi.org/10.5281/zenodo.14259611> (last
access: 2 December 2024).

Data availability. The surface layer measurements are obtained from the Antarctic Meteorological Research Center and the Automatic
Weather Station program (<ftp://amrc.ssec.wisc.edu/pub/aws/q3h/2015>, last access: 16 July 2023). The meteorological parameters measured
by the radiosondes at McMurdo and South Pole are available at the Antarctic Meteorological Research Center (<ftp://amrc.ssec.wisc.edu/pub>,
475 last access: 16 July 2023), while the meteorological fields at Dome C are available at the Antarctic Meteo-Climatological Observatory
(<http://www.climantartide.it>, last access: 16 July 2023). ERA5 data are obtained (<https://cds.climate.copernicus.eu>, last access: 16 July 2023).

Author contributions. QY and CZ designed the study. QY collected data on the field. QY, GL, and JF ran the simulations. QY performed the
analysis and wrote the first draft of the manuscript. QY, CZ, JF, GL, JG, ZX, MX, and ZY discussed and revised the manuscript

Competing interests. The authors declare that they have no conflict of interest.

480 *Acknowledgements.* This research was supported by the Strategic Priority Research Program of Chinese Academy of Sciences (XDB0500303),
the National Key Research and Development Program of China (2022YFC3700701), the USTC Research Funds of the Double First-Class
Initiative (YD2080002007, KY2080000114), the Fundamental Research Funds for the Central Universities (WK2080000192), the China
Postdoctoral Science Foundation (2023M743355), Postdoctoral Fellowship Program of CPSF (GZB20230699), the Natural Science Founda-
tion of Anhui (2208085UQ09, 2208085UQ02), the Science and Technology Innovation Project of Laoshan Laboratory (LSKJ202300305).
485 This study used computing resources from the Supercomputing Center of the University of Science and Technology of China (USTC), the

<https://doi.org/10.5194/gmd-2024-229>
Preprint. Discussion started: 24 January 2025
© Author(s) 2025. CC BY 4.0 License.



National Key Scientific and Technological Infrastructure project “Earth System Numerical Simulation Facility” (EarthLab), and the Qingdao Supercomputing and Big Data Center.



References

- Argentini, S. and Mastrantonio, G.: Barrier winds recorded during two summer Antarctic campaigns and their interaction with the katabatic flows as observed by a tri-axial Doppler sodar, *International Journal of Remote Sensing*, 15, 455–466, <https://doi.org/10.1080/01431169408954086>, 1994.
- Balaji, V., Boville, B., and Samson Cheung, e. a.: ESMF User's Guide, https://earthsystemmodeling.org/docs/release/latest/ESMF_usrdoc.pdf, accessed: 2024-09-29, 2024.
- Bromwich, D. H., Monaghan, A. J., Manning, K. W., and Powers, J. G.: Real-Time Forecasting for the Antarctic: An Evaluation of the Antarctic Mesoscale Prediction System (AMPS), *Monthly Weather Review*, 133, 579 – 603, <https://doi.org/10.1175/MWR-2881.1>, 2005.
- Clem, K. R., Fogt, R. L., Turner, J., Lintner, B. R., Marshall, G. J., Miller, J. R., and Renwick, J. A.: Record warming at the South Pole during the past three decades, *Nature Climate Change*, 10, 762–770, <https://doi.org/10.1038/s41558-020-0815-z>, 2020.
- Collins, S. N., James, R. S., Ray, P., Chen, K., Lassman, A., and Brownlee, J.: Grids in Numerical Weather and Climate Models, in: *Climate Change and Regional/Local Responses*, edited by Zhang, Y. and Ray, P., chap. 4, IntechOpen, Rijeka, <https://doi.org/10.5772/55922>, 2013.
- Douville, H.: Robust and perfectible constraints on human-induced Arctic amplification, *Communications Earth and Environment*, 4, 283, <https://doi.org/10.1038/s43247-023-00949-5>, 2023.
- Dudhia, J., Skamarock, W. C., and Klemp, J. B.: Conservative Split-Explicit Time Integration Methods for the Compressible Nonhydrostatic Equations, *Monthly Weather Review*, 135, 2897–2913, <https://doi.org/10.1175/mwr3440.1>, 2007.
- Feng, J., Zhao, C., Du, Q., Xu, M., Gu, J., Hu, Z., and Chen, Y.: Simulating Atmospheric Dust With a Global Variable-Resolution Model: Model Description and Impacts of Mesh Refinement, *Journal of Advances in Modeling Earth Systems*, 15, <https://doi.org/10.1029/2023ms003636>, 2023.
- Fréville, H., Brun, E., Picard, G., Tatarinova, N., Arnaud, L., Lanconelli, C., Reijmer, C., and van den Broeke, M.: Using MODIS land surface temperatures and the Crocus snow model to understand the warm bias of ERA-Interim reanalyses at the surface in Antarctica, *The Cryosphere*, 8, 1361–1373, <https://doi.org/10.5194/tc-8-1361-2014>, 2014.
- Gao, K., Duan, A., Chen, D., and Wu, G.: Surface energy budget diagnosis reveals possible mechanism for the different warming rate among Earth's three poles in recent decades, *Science Bulletin*, 64, 1140–1143, <https://doi.org/https://doi.org/10.1016/j.scib.2019.06.023>, 2019.
- Golledge, N. R., Kowalewski, D. E., Naish, T. R., Levy, R. H., Fogwill, C. J., and Gasson, E. G.: The multi-millennial Antarctic commitment to future sea-level rise, *Nature*, 526, 421–5, <https://doi.org/10.1038/nature15706>, golledge, N R Kowalewski, D E Naish, T R Levy, R H Fogwill, C J Gasson, E G W eng Research Support, Non-U.S. Gov't Research Support, U.S. Gov't, Non-P.H.S. England 2015/10/16 Nature. 2015 Oct 15;526(7573):421-5. doi: 10.1038/nature15706., 2015.
- Grell, G. A. and Freitas, S. R.: A scale and aerosol aware stochastic convective parameterization for weather and air quality modeling, *Atmospheric Chemistry and Physics*, 14, 5233–5250, <https://doi.org/10.5194/acp-14-5233-2014>, 2014.
- Gu, J., Feng, J., Hao, X., Fang, T., Zhao, C., An, H., Chen, J., Xu, M., Li, J., Han, W., Yang, C., Li, F., and Chen, D.: Establishing a non-hydrostatic global atmospheric modeling system at 3-km horizontal resolution with aerosol feedbacks on the Sunway supercomputer of China, *Science Bulletin*, 67, 1170–1181, <https://doi.org/https://doi.org/10.1016/j.scib.2022.03.009>, 2022.
- Gu, J., Zhao, C., Xu, M., Feng, J., Li, G., Zhao, Y., Hao, X., Chen, J., and An, H.: Global convection-permitting model improves subseasonal forecast of plum rain around Japan, *Environmental Research Letters*, 19, 104021, <https://doi.org/10.1088/1748-9326/ad71e2>, 2024.
- Ha, S., Duda, M. G., Skamarock, W. C., and Park, S.-H.: Limited-Area Atmospheric Modeling Using an Unstructured Mesh, *Monthly Weather Review*, 146, 3445–3460, <https://doi.org/10.1175/mwr-d-18-0155.1>, 2018.



- 525 Hagelin, S., Masciadri, E., Lascaux, F., and Stoesz, J.: Comparison of the atmosphere above the South Pole, Dome C and Dome A: first attempt, *Monthly Notices of the Royal Astronomical Society*, 387, 1499–1510, <https://doi.org/10.1111/j.1365-2966.2008.13361.x>, 2008.
- Hao, X., Fang, T., Chen, J., Gu, J., Feng, J., An, H., and Zhao, C.: swMPAS-A: Scaling MPAS-A to 39 Million Heterogeneous Cores on the New Generation Sunway Supercomputer, *IEEE Transactions on Parallel and Distributed Systems*, 34, 141–153, <https://doi.org/10.1109/TPDS.2022.3215002>, 2023.
- 530 Hersbach, H., Bell, B., Berrisford, P., Hirahara, S., Horányi, A., Muñoz-Sabater, J., Nicolas, J., Peubey, C., Radu, R., Schepers, D., Simmons, A., Soci, C., Abdalla, S., Abellan, X., Balsamo, G., Bechtold, P., Biavati, G., Bidlot, J., Bonavita, M., De Chiara, G., Dahlgren, P., Dee, D., Diamantakis, M., Dragani, R., Flemming, J., Forbes, R., Fuentes, M., Geer, A., Haimberger, L., Healy, S., Hogan, R. J., Hólm, E., Janisková, M., Keeley, S., Laloyaux, P., Lopez, P., Lupu, C., Radnoti, G., de Rosnay, P., Rozum, I., Vamborg, F., Villaume, S., and Thépaut, J.: The ERA5 global reanalysis, *Quarterly Journal of the Royal Meteorological Society*, 146, 1999–2049, <https://doi.org/10.1002/qj.3803>,
535 2020.
- Hortal, M. and Simmons, A.: Use of Reduced Gaussian Grids in Spectral Models, *Monthly Weather Review*, 119, 1057–1074, 1991.
- Hsu, L.-H., Tseng, L.-S., Hou, S.-Y., Chen, B.-F., and Sui, C.-H.: A Simulation Study of Kelvin Waves Interacting with Synoptic Events during December 2016 in the South China Sea and Maritime Continent, *Journal of Climate*, 33, 6345–6359, <https://doi.org/10.1175/jcli-d-20-0121.1>, 2020.
- 540 Iacono, M. J., Delamere, J. S., Mlawer, E. J., Shephard, M. W., Clough, S. A., and Collins, W. D.: Radiative forcing by long-lived greenhouse gases: Calculations with the AER radiative transfer models, *Journal of Geophysical Research: Atmospheres*, 113, <https://doi.org/https://doi.org/10.1029/2008JD009944>, 2008.
- Imberger, M., Larsén, X. G., and Davis, N.: Investigation of Spatial and Temporal Wind-Speed Variability During Open Cellular Convection with the Model for Prediction Across Scales in Comparison with Measurements, *Boundary-Layer Meteorology*, 179, 291–312,
545 <https://doi.org/10.1007/s10546-020-00591-0>, 2021.
- Ju, L., Ringler, T., and Gunzburger, M.: Voronoi Tessellations and Their Application to Climate and Global Modeling, pp. 313–342, Springer Berlin Heidelberg, Berlin, Heidelberg, https://doi.org/10.1007/978-3-642-11640-7_10, 2011.
- Kannemadugu, H. B. S., Sudhakaran Syamala, P., Taori, A., Bothale, R. V., and Chauhan, P.: Atmospheric aerosol optical properties and trends over Antarctica using in-situ measurements and MERRA-2 aerosol products, *Polar Science*, 38, 101011,
550 <https://doi.org/https://doi.org/10.1016/j.polar.2023.101011>, research Advances from Larsemann Hills, Antarctica: International Cooperation and Future Prospects - Part 1, 2023.
- Kessenich, H. E., Seppala, A., and Rodger, C. J.: Potential drivers of the recent large Antarctic ozone holes, *Nat Commun*, 14, 7259, <https://doi.org/10.1038/s41467-023-42637-0>, kessenich, Hannah E Seppala, Annika Rodger, Craig J eng UOOX2106/Ministry of Business, Innovation and Employment (MBIE)/England 2023/11/22 Nat Commun. 2023 Nov 21;14(1):7259. doi: 10.1038/s41467-023-42637-0., 2023.
555 0., 2023.
- Klemp, J. B.: A Terrain-Following Coordinate with Smoothed Coordinate Surfaces, *Monthly Weather Review*, 139, 2163–2169, <https://doi.org/10.1175/mwr-d-10-05046.1>, 2011.
- Lazzara, M. A., Weidner, G. A., Keller, L. M., Thom, J. E., and Cassano, J. J.: Antarctic Automatic Weather Station Program: 30 Years of Polar Observation, *Bulletin of the American Meteorological Society*, 93, 1519–1537, <https://doi.org/10.1175/bams-d-11-00015.1>, 2012.
- 560 Lui, Y. S., Tse, L. K. S., Tam, C.-Y., Lau, K. H., and Chen, J.: Performance of MPAS-A and WRF in predicting and simulating western North Pacific tropical cyclone tracks and intensities, *Theoretical and Applied Climatology*, 143, 505–520, <https://doi.org/10.1007/s00704-020-03444-5>, 2020.



- Ma, Y., Bian, L., Xiao, C., Allison, I., and Zhou, X.: Near surface climate of the traverse route from Zhongshan Station to Dome A, East Antarctica, *Antarctic Science*, 22, 443–459, <https://doi.org/10.1017/s0954102010000209>, 2010.
- 565 Nakanishi, M. and Niino, H.: An improved Mellor–Yamada level-3 model: its numerical stability and application to a regional prediction of advection fog, *Boundary-Layer Meteorology*, 119, 397–407, <https://doi.org/10.1023/B:BOUN.0000020164.04146.98>, 2006.
- Núñez Ocasio, K. M. and Rios-Berrios, R.: African Easterly Wave Evolution and Tropical Cyclogenesis in a Pre-Helene (2006) Hind-cast Using the Model for Prediction Across Scales-Atmosphere (MPAS-A), *Journal of Advances in Modeling Earth Systems*, 15, <https://doi.org/10.1029/2022ms003181>, 2023.
- 570 O’Connor, W. P. and Bromwich, D. H.: Surface airflow around Windless Bight, Ross Island, Antarctica, *Quarterly Journal of the Royal Meteorological Society*, 114, 917–938, <https://api.semanticscholar.org/CorpusID:140173495>, 1988.
- Parish, T. R. and Cassano, J. J.: The Role of Katabatic Winds on the Antarctic Surface Wind Regime, *Monthly Weather Review*, 131, 317–333, 2001.
- Petit, J. R., Jouzel, J., Raynaud, D., Barkov, N. I., Barnola, J. M., Basile, I., Bender, M., Chappellaz, J., Davis, M., Delaygue, G., Delmotte, M., Kotlyakov, V. M., Legrand, M., Lipenkov, V. Y., Lorius, C., Pépin, L., Ritz, C., Saltzman, E., and Stievenard, M.: Climate and atmospheric history of the past 420,000 years from the Vostok ice core, Antarctica, *Nature*, 399, 429–436, <https://doi.org/10.1038/20859>, 1999.
- Pilon, R., Zhang, C., and Dudhia, J.: Roles of deep and shallow convection and microphysics in the MJO simulated by the Model for Prediction Across Scales, *Journal of Geophysical Research: Atmospheres*, 121, <https://doi.org/10.1002/2015jd024697>, 2016.
- 580 Ringler, T., Ju, L., and Gunzburger, M.: A multiresolution method for climate system modeling: application of spherical centroidal Voronoi tessellations, *Ocean Dynamics*, 58, 475–498, <https://doi.org/10.1007/s10236-008-0157-2>, 2008.
- Ringler, T. D., Thuburn, J., Klemp, J. B., and Skamarock, W. C.: A unified approach to energy conservation and potential vorticity dynamics for arbitrarily-structured C-grids, *Journal of Computational Physics*, 229, 3065–3090, <https://doi.org/10.1016/j.jcp.2009.12.007>, 2010.
- Ringler, T. D., Jacobsen, D., Gunzburger, M., Ju, L., Duda, M., and Skamarock, W.: Exploring a Multiresolution Modeling Approach within the Shallow-Water Equations, *Monthly Weather Review*, 139, 3348–3368, <https://doi.org/10.1175/mwr-d-10-05049.1>, 2011.
- 585 Rinke, A., Ma, Y., Bian, L., Xin, Y., Dethloff, K., Persson, P. O. G., Lüpkes, C., and Xiao, C.: Evaluation of atmospheric boundary layer-surface process relationships in a regional climate model along an East Antarctic traverse, *Journal of Geophysical Research: Atmospheres*, 117, n/a–n/a, <https://doi.org/10.1029/2011jd016441>, 2012.
- Schwartz, C. S.: Medium-Range Convection-Allowing Ensemble Forecasts with a Variable-Resolution Global Model, *Monthly Weather Review*, 147, 2997–3023, <https://doi.org/10.1175/mwr-d-18-0452.1>, 2019.
- 590 Silber, I., Verlinde, J., Wang, S.-H., Bromwich, D. H., Fridlind, A. M., Cadeddu, M., Eloranta, E. W., and Flynn, C. J.: Cloud Influence on ERA5 and AMPS Surface Downwelling Longwave Radiation Biases in West Antarctica, *Journal of Climate*, 32, 7935 – 7949, <https://doi.org/10.1175/JCLI-D-19-0149.1>, 2019.
- Skamarock, W. C., Klemp, J. B., Dudhia, J., Gill, D. O., Barker, D., Duda, M. G., . . . , and Powers, J. G.: A Description of the Advanced Research WRF Version 3 (No. NCAR/TN-475+STR), Report, University Corporation for Atmospheric Research, <https://doi.org/10.5065/D68S4MVH>, 2008.
- 595 Skamarock, W. C., Klemp, J. B., Duda, M. G., Fowler, L. D., Park, S.-H., and Ringler, T. D.: A Multiscale Nonhydrostatic Atmospheric Model Using Centroidal Voronoi Tessellations and C-Grid Staggering, *Monthly Weather Review*, 140, 3090–3105, <https://doi.org/10.1175/mwr-d-11-00215.1>, 2012.



- 600 Tewari, M., Wang, W., Dudhia, J., LeMone, M., Mitchell, K., Ek, M., Gayno, G., Wegiel, J., and Cuenca, R.: Implementation and verification of the united NOAA land surface model in the WRF model, pp. 11–15, 2016.
- Thompson, G., Field, P. R., Rasmussen, R. M., and Hall, W. D.: Explicit Forecasts of Winter Precipitation Using an Improved Bulk Microphysics Scheme. Part II: Implementation of a New Snow Parameterization, *Monthly Weather Review*, 136, 5095 – 5115, <https://doi.org/10.1175/2008MWR2387.1>, 2008.
- 605 Thuburn, J., Ringler, T. D., Skamarock, W. C., and Klemp, J. B.: Numerical representation of geostrophic modes on arbitrarily structured C-grids, *Journal of Computational Physics*, 228, 8321–8335, <https://doi.org/10.1016/j.jcp.2009.08.006>, 2009.
- Wadham, J. L., Hawkings, J. R., Tarasov, L., Gregoire, L. J., Spencer, R. G. M., Gutjahr, M., Ridgwell, A., and Kohfeld, K. E.: Ice sheets matter for the global carbon cycle, *Nat Commun*, 10, 3567, <https://doi.org/10.1038/s41467-019-11394-4>, 2019.
- Wang, S.-m., Xie, A.-h., and Zhu, J.-p.: Does polar amplification exist in Antarctic surface during the recent four decades?, *Journal of Mountain Science*, 18, 2626–2634, <https://doi.org/10.1007/s11629-021-6912-2>, 2021.
- 610 Wicker, L. J. and Skamarock, W. C.: Time-Splitting Methods for Elastic Models Using Forward Time Schemes, *Monthly Weather Review*, 130, 2088–2097, [https://doi.org/10.1175/1520-0493\(2002\)130<2088:TSMFEM>2.0.CO;2](https://doi.org/10.1175/1520-0493(2002)130<2088:TSMFEM>2.0.CO;2), 2002.
- Wille, J. D., Bromwich, D. H., Nigro, M. A., Cassano, J. J., Mateling, M., Lazzara, M. A., and Wang, S.-H.: Evaluation of the AMPS Boundary Layer Simulations on the Ross Ice Shelf with Tower Observations, *Journal of Applied Meteorology and Climatology*, 55, 2349 – 2367, <https://doi.org/10.1175/JAMC-D-16-0032.1>, 2016.
- 615 Xu, M., Zhao, C., Gu, J., Feng, J., Hagos, S., Leung, L. R., Luo, Y., Guo, J., Li, R., and Fu, Y.: Convection-Permitting Hindcasting of Diurnal Variation of Mei-yu Rainfall Over East China With a Global Variable-Resolution Model, *Journal of Geophysical Research: Atmospheres*, 126, e2021JD034823, <https://doi.org/10.1029/2021JD034823>, e2021JD034823 2021JD034823, 2021.
- Xu, M., Zhao, C., Li, G., Gu, J., Feng, J., Zhang, Z., and Guo, J.: Modeling Across Scales of Heavy Precipitation With a Global Variable-Resolution Model: A Case Study of a Catastrophic Event in China, *Journal of Geophysical Research: Atmospheres*, 129, e2024JD041180, <https://doi.org/10.1029/2024JD041180>, e2024JD041180 2024JD041180, 2024.
- 620 Yang, Q., Wu, X., Han, Y., Qing, C., Wu, S., Su, C., Wu, P., Luo, T., and Zhang, S.: Estimating the astronomical seeing above Dome A using Polar WRF based on the Tatarskii equation, *Opt. Express*, 29, 44 000–44 011, <https://doi.org/10.1364/OE.439819>, 2021a.
- Yang, Q., Wu, X., Han, Y., Qing, C., Wu, S., Su, C., Wu, P., and Zhang, S.: Model for estimating the astronomical seeing at Dome A, Antarctica, *Opt. Express*, 29, 35 238–35 246, <https://doi.org/10.1364/OE.439816>, 2021b.
- 625 Yang, Q., Wu, X., Wang, Z., Hu, X., Guo, Y., and Qing, C.: Simulating the night-time astronomical seeing at Dome A using Polar WRF, *Monthly Notices of the Royal Astronomical Society*, 515, 1788–1794, <https://doi.org/10.1093/mnras/stac1930>, 2022.
- Yang, Q., Wu, X., Hu, X., Wang, Z., Qing, C., Luo, T., Wu, P., Qian, X., and Guo, Y.: Antarctic atmospheric Richardson number from radiosonde measurements and AMPS, *Atmospheric Chemistry and Physics*, 23, 6339–6355, <https://doi.org/10.5194/acp-23-6339-2023>, 2023a.
- 630 Yang, Q., Wu, X., Qing, C., Luo, T., Li, X., Cui, S., Wu, P., Qian, X., Wang, Z., Hu, X., Guo, Y., Yan, C., and Qiao, Z.: Discovery of Calm Astronomical Sites Over the Antarctic Continent, *The Astronomical Journal*, 165, 158, <https://doi.org/10.3847/1538-3881/acbb02>, 2023b.
- Zentek, R. and Heinemann, G.: Verification of the regional atmospheric model CCLM v5.0 with conventional data and lidar measurements in Antarctica, *Geoscientific Model Development*, 13, 1809–1825, <https://doi.org/10.5194/gmd-13-1809-2020>, 2020.
- 635 Zhang, S., Xu, S., Fu, H., Wu, L., Liu, Z., Gao, Y., Zhao, C., Wan, W., Wan, L., Lu, H., Li, C., Liu, Y., Lv, X., Xie, J., Yu, Y., Gu, J., Wang, X., Zhang, Y., Ning, C., Fei, Y., Guo, X., Wang, Z., Wang, X., Wang, Z., Qu, B., Li, M., Zhao, H., Jiang, Y., Yang, G., Lu, L., Wang, H., An, H., Zhang, X., Zhang, Y., Ma, W., Yu, F., Xu, J., Lin, X., and Shen, X.: Toward Earth system modeling with resolved clouds



- and ocean submesoscales on heterogeneous many-core HPCs, *Natl Sci Rev*, 10, nwad069, <https://doi.org/10.1093/nsr/nwad069>, zhang, Shaoqing Xu, Shiming Fu, Haohuan Wu, Lixin Liu, Zhao Gao, Yang Zhao, Chun Wan, Wubing Wan, Lingfeng Lu, Haitian Li, Chenling
- 640 Liu, Yanfei Lv, Xiaojing Xie, Jiayu Yu, Yangyang Gu, Jun Wang, Xuanton Zhang, Yan Ning, Chenhui Fei, Yunlong Guo, Xiuwen Wang, Zhaoying Wang, Xue Wang, Zhenming Qu, Binglin Li, Mingkui Zhao, Haoran Jiang, Yingjing Yang, Guang Lu, Lv Wang, Hong An, Hong Zhang, Xin Zhang, Yu Ma, Wentao Yu, Fujiang Xu, Jing Lin, Xiaopei Shen, *Xueshun eng China* 2023/05/14 *Natl Sci Rev*. 2023 Mar 20;10(6):nwad069. doi: 10.1093/nsr/nwad069. eCollection 2023 Jun., 2023.
- 645 Zhao, C., Xu, M., Wang, Y., Zhang, M., Guo, J., Hu, Z., Leung, L. R., Duda, M., and Skamarock, W.: Modeling extreme precipitation over East China with a global variable-resolution modeling framework (MPASv5.2): impacts of resolution and physics, *Geoscientific Model Development*, 12, 2707–2726, <https://doi.org/10.5194/gmd-12-2707-2019>, 2019.